ACS NANO

www.acsnano.org

High-Efficiency N_2 Electroreduction Enabled by Se-Vacancy-Rich WSe_{2-x} in Water-in-Salt Electrolytes

Peng Shen, Xingchuan Li, Yaojing Luo, Yali Guo, Xiaolin Zhao, and Ke Chu*

Cite This: https://doi.org/10.1021/acsnano.2c00596 **Read Online**

ACCESS | Metrics & More | Article Recommendations | Supporting Information

ABSTRACT: Electrocatalytic nitrogen reduction reaction (NRR) is a promising approach for renewable NH_3 production, while developing the NRR electrocatalysis systems with both high activity and selectivity remains a significant challenge. Herein, we combine catalyst and electrolyte engineering to achieve a high-efficiency NRR enabled by a Se-vacancy-rich WSe_{2-x} catalyst in water-in-salt electrolyte (WISE). Extensive characterizations, theoretical calculations, and in situ X-ray photoelectron/Raman spectroscopy reveal that WISE ensures suppressed H_2 evolution, improved N_2 affinity on the catalyst surface, as well as an enhanced π-back-donation ability of active sites, thereby promoting both activity and selectivity for the NRR. As a result, an excellent faradaic efficiency of 62.5% and NH_3 yield of 181.3 μg h^{-1} mg^{-1} is achieved with WSe_{2-x} in 12 m $LiClO_4$, which is among the highest NRR performances reported to date.

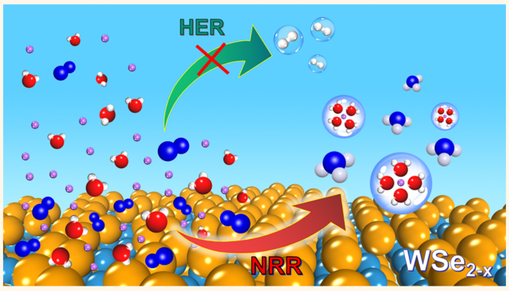

KEYWORDS: *electrocatalytic reduction reaction, water-in-salt electrolytes, density functional theory calculations, molecular dynamics simulations, in situ spectroscopy*

INTRODUCTION

Ammonia (NH_3), a vital chemical with high energy density, is of great importance for food production and clean energy exploration.[1] Commercial NH_3 synthesis is dominated by the Haber−Bosch process under harsh synthetic conditions, leading to huge energy consumption and large carbon dioxide emissions.[2] Promisingly, electrochemical dinitrogen reduction reaction (NRR) has been recognized as an appealing approach for renewable NH_3 synthesis.[3−9] Currently, a large energy barrier for the cleavage of a strong N≡N bond and the competing hydrogen evolution reaction (HER), as two fundamental obstacles, severely hamper an efficient NRR process.[3−5] To promote NRR efficiency, high-performing catalysts are required to reduce the energy barriers for N≡N dissociation and impede the unwanted HER simultaneously.[10]

Diverse groups of precious metals,[11−13] transition metal compounds,[14−16] and metal-free materials[17−19] have been explored as NRR catalysts, with their performance further improved by several strategies of defect engineering,[20−25] heteroatom doping,[26−28] and heterostructure coupling.[29−31] Despite significant progress made in catalyst exploration, it still remains a significant challenge to develop the desired catalysts with both high activity and selectivity for the NRR.[32−34] A major challenge for high-efficiency NRR electrocatalysis lies in the suppression of the parasitic HER in aqueous electrolytes.[3,33] Compared to conventional catalyst design,[35−37] the electrolyte engineering may offer a more straightforward approach to realize sufficient HER inhibition. Previous reports have demonstrated that nonaqueous ionic liquids with high N_2 solubility and limited proton supply can largely impede the HER.[38,39] An excellent faradaic efficiency (FE) of 60% was obtained on an Fe-based catalyst in a $[P_{6,6,6,14}]$[eFAP] ionic liquid electrolyte.[39] However, the high viscosity of ionic liquids also hinders effective N_2 mass transfer, which can cause decreased N_2 accessibility on the catalyst and thus an unsatisfactory NH_3 yield rate.[38] Very recently, a molecular crowding aqueous electrolyte containing poly(ethylene glycol) (PEG) was employed for the NRR,[40] where PEG can interrupt the hydrogen bonding network of water molecules to retard the HER kinetics. With this electrolyte, a high FE of 32.13% was achieved on a TiO_2 nanoarray. Nevertheless, this FE still falls short of the practical requirement and needs further improvement. Water-in-salt electrolytes (WISEs), built with

Received: January 18, 2022
Accepted: April 18, 2022

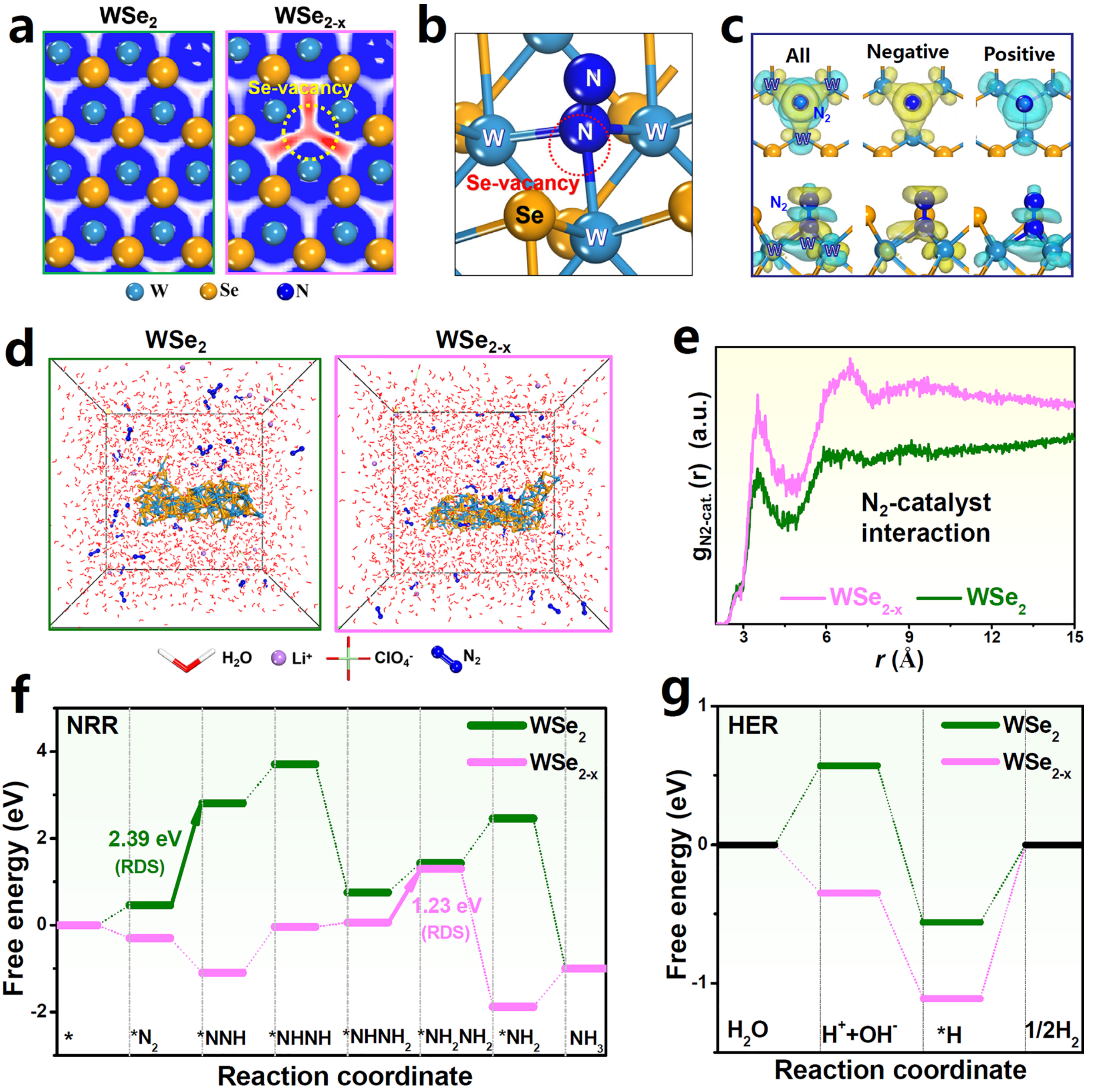

Figure 1. (a) Electron location function images of WSe$_2$ and WSe$_{2-x}$ sliced along the (001) plane. Red, electron accumulation; blue, electron depletion. (b) Optimized structure of absorbed N$_2$ on a Se vacancy site and its corresponding (c) differential charge density (top, top view; bottom, side view). Yellow, electron accumulation; cyan, electron depletion. (d) Snapshots for the dynamic process of N$_2$ adsorption on WSe$_2$ and WSe$_{2-x}$ after 5 ns MD simulations and corresponding (e) radial distribution function curves of N$_2$−catalyst interaction. (f) Free energy diagram of preferred alternating NRR pathway on WSe$_2$ and WSe$_{2-x}$. (g) Free energy diagram of HER pathway on WSe$_2$ and WSe$_{2-x}$ in neutral media.

superconcentrated aqueous electrolytes (salt/solvent ratio >1 by weight), have recently attracted widespread attention for use in aqueous batteries due to the special solvation structures of WISEs to prevent dendritic metal formation caused by water decomposition.[41−43] In WISEs, most of the water molecules are strongly confined with abundant cations in the solvation sheaths, and thus the HER process would be substantially restricted due to the shortage of free water molecules and minimized water activity.[42] In this respect, electrolyte engineering by replacing conventional dilute electrolytes (DEs) with WISEs may provide a very promising strategy to effectively suppress the competing HER and enhance the NRR.[3,44]

Herein, the catalyst and electrolyte engineering are rationally combined to realize a high-efficiency NRR. The developed Se-vacancy-rich WSe$_{2-x}$ catalyst in a WISE (12 m LiClO$_4$) exhibits an excellent FE of 62.5% with an NH$_3$ yield of 181.3 μg h^{-1} mg^{-1}, surpassing nearly all of the current state-of-the-art NRR catalyst systems. The catalyst/electrolyte design principles and the NRR mechanism in WISE are investigated by density functional theory (DFT) calculations, molecular dynamics (MD) simulations, and in situ X-ray photoelectron/Raman spectroscopy.

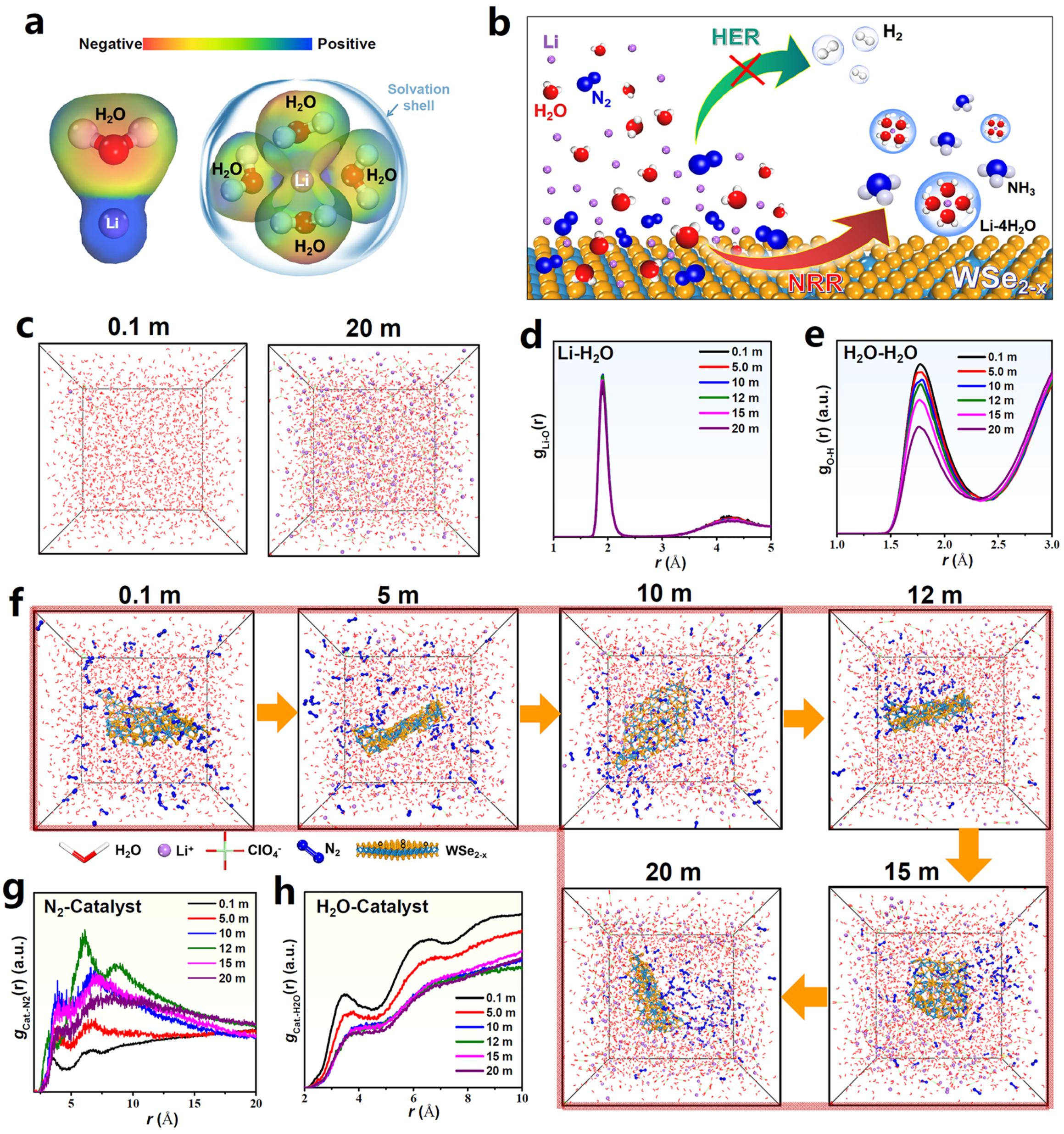

Figure 2. (a) ESP of Li−H$_2$O and Li−4H$_2$O interactions. (b) Schematic of the NRR process in WISE. (c) Snapshots for the 0.1 and 20 m LiClO$_4$ electrolytes after 5 ns MD simulations. (d,e) RDF curves of Li−H$_2$O and H$_2$O−H$_2$O interactions at different concentrations of electrolytes. (f) Snapshots for the dynamic process of N$_2$ adsorption on WSe$_{2-x}$ at different concentrations of electrolytes and corresponding (g,h) RDF curves of N$_2$−catalyst and H$_2$O−catalyst interactions.

RESULTS AND DISCUSSION

Theoretical calculations are first performed to guide the rational design of a catalyst and an electrolyte. First, the NRR efficiency of the WSe$_{2-x}$ catalyst is evaluated by DFT/MD computations. WSe$_{2-x}$ shows the delocalized electrons accumulating at the Se vacancy region (Figure 1a and Figure S1), and N$_2$ can be favorably trapped into the Se vacancy and bonded with three unsaturated W atoms (W−W−W trimer, Figure 1b and Figure S2). The charge density difference (Figure 1b) presents high-density charge accumulation and depletion around both *N$_2$ and the W−W−W trimer, indicating the efficient N$_2$ activation over the W−W−W trimer through an "acceptance donation" mechanism (Figure S2c).[45] The effective N$_2$ adsorption on WSe$_{2-x}$ can also be verified by MD simulations (Figure S3), displaying more N$_2$ accumulation on WSe$_{2-x}$ (Figure 1d) with a stronger N$_2$−catalyst interaction (Figure 1e) with respect to WSe$_2$ counterparts. The favorable N$_2$ adsorption on WSe$_{2-x}$ would facilitate the formation of *N$_2$H, a key intermediate that governs the protonation process (Figures S4 and S5).[46] Meanwhile, WSe$_{2-x}$ exhibits a smaller band gap and lower work function compared to WSe$_2$ (Figure S6), in favor of boosting the NRR kinetics by accelerating the charge transport.[47]

The entire free energy diagram displays that, due to the strong N$_2$ activation over the Se vacancy, WSe$_{2-x}$ shows an energetic downhill path for the initial *N$_2$ → *N$_2$H (Figure 1f), whereas *N$_2$H formation on WSe$_2$ needs to overcome a high energetic barrier of 2.39 eV. Afterward, the protonation of *N$_2$H prefers to adopt an alternative pathway for both WSe$_2$ and WSe$_{2-x}$ (Figures S7 and S8), where WSe$_{2-x}$ exhibits a rate-

https://doi.org/10.1021/acsnano.2c00596

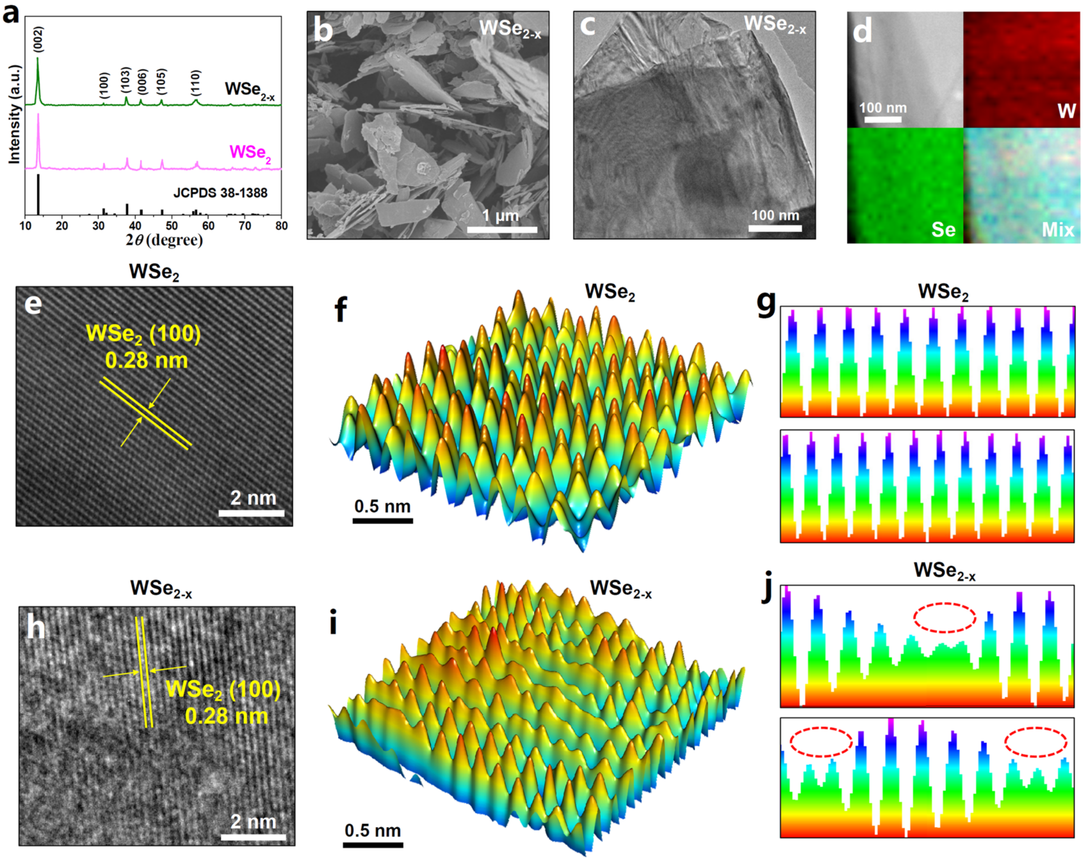

Figure 3. (a) XRD patterns of WSe_2 and WSe_{2-x}. (b,c) SEM/TEM images of WSe_{2-x}. (d) Element mapping images of WSe_{2-x}. (e,h) HRTEM images of WSe_2/WSe_{2-x}. (f,i) 3D topographic atom imaging profiles of WSe_2/WSe_{2-x} and corresponding (g,j) lattice line scanning analyses.

determining step (RDS) energy barrier of 1.23 eV for $*NHNH_2 \rightarrow *NH_2NH_2$, which is much lower than that of WSe_2 (2.39 eV for $*N_2 \rightarrow *N_2H$), indicating the considerably enhanced NRR energetics over WSe_{2-x}. Unfortunately, WSe_{2-x} also exhibits a strong tendency for H_2O dissociation (−0.36 eV for $H_2O \rightarrow H^+ + OH^-$, Figure 1g), which favors the HER and retards the NRR. To suppress the HER on WSe_{2-x}, an electrolyte engineering strategy using WISEs is adopted.

Li-based electrolytes have been extensively applied for the NRR.[48−51] In a Li electrolyte, the electrostatic surface potential (ESP) diagrams (Figure 2a) show that the electron-concentrated O atom of H_2O tends to coordinate with the electron-deficient Li cation by coulombic interactions,[42] and one central Li cation can be preferentially coordinated with four neighboring H_2O molecules to form a rigid solvation sheath structure (Figure S9). Therefore, in WISEs, most H_2O molecules would be trapped in Li-mediated solvation sheaths, which substantially reduces the number of free H_2O molecules to weaken the water activity and dissociation, thus facilitating the suppressed HER and promoted NRR, as illustrated in Figure 2b. We then employ MD simulations to investigate the solvation effect and NRR activity of WSe_{2-x} at different concentrations of $LiClO_4$ prototype electrolytes. After simulation, the snapshots (Figure 2c and Figure S10) show that the electrolyte structure is highly uniform at different electrolyte concentrations (C). The corresponding radial distribution function (RDF, Figure 2d) of these electrolytes shows a sharp peak at 1.9 Å, which is assigned to $Li-H_2O$ coordinated interaction in the primary solvation sheath and is nearly independent of the electrolyte concentration.[52] Apparently, the increased electrolyte concentration can progressively lower the activity of H_2O molecules by confining them in solvation sheaths (Figure 2e), highlighting the prominent solvation effect of WISE in suppressing the HER.

With introducing only N_2 in the electrolytes (Figure S11), the N_2 molecules are uniformly distributed at all concentrations, and the above solvation effect remains. However, with additionally introducing the WSe_{2-x} catalyst, the N_2 distribution delivers a noticeable dependence on the electrolyte concentration (Figure 2f), where a high density of N_2 accumulated on the catalyst can be observed at $C \geq 12$ m. Quantitative RDF analysis (Figure 2g) reveals that the N_2−catalyst interactions increase with electrolyte concentration and reach the maximum at $C = 12$ m (Figure S12). The reduced N_2−catalyst interactions at $C > 12$ m can be explained by the very low N_2 diffusion rate at very high concentrations (Figure S13), which restricts the N_2 transport to the catalyst surface. Meanwhile, the H_2O−catalyst interactions decrease first and remain nearly constant at $C \geq 10$ m (Figure 2h and Figure S12). Therefore, the optimum $LiClO_4$ electrolyte concentration can be determined to be $C = 12$ m, at which the catalyst shows the strongest N_2 affinity on the catalyst surface along with the minimal influence by H_2O and thus is favorable for high catalytic selectivity toward N_2 electroreduction.

Guided by the above DFT and MD investigations, we carry out the proof-of-concept experiments. A liquid-phase exfoliation method was used to fabricate WSe_2 nanosheets, which were further annealed under mixed Ar/H_2 atmosphere to create enriched Se vacancies, obtaining WSe_{2-x} nanosheets

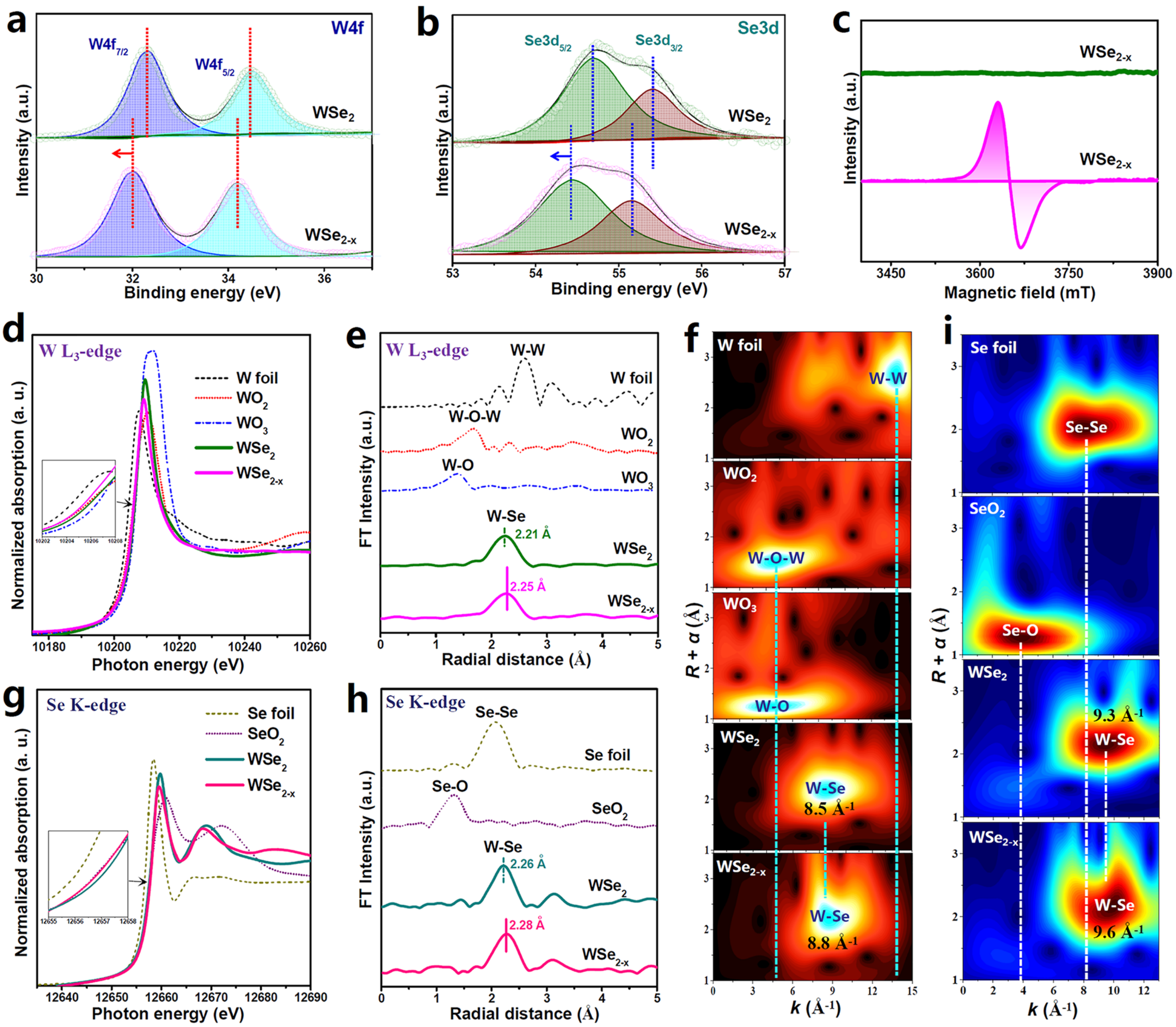

Figure 4. (a,b) XPS W 4f/Se 3d spectra of WSe_2 and WSe_{2-x}. (c) EPR spectra of WSe_2 and WSe_{2-x}. (d) W L_3-edge XANES and corresponding (e) EXAFS spectra and (f) WT contour maps of WSe_2, WSe_{2-x}, and reference samples of W foil, WO_2, and WO_3. (g) Se K-edge XANES and corresponding (h) EXAFS spectra and (i) WT contour maps of WSe_2, WSe_{2-x}, and reference samples of Se foil and SeO_2.

(Figure S14). The X-ray diffraction (XRD, Figure 3a) patterns of both WSe_2 and WSe_{2-x} show the characteristic peaks of hexagonal WSe_2 (JCPDS No. 38-1388). Scanning electron microscopy (SEM, Figure 3b) and transmission electron microscopy (TEM, Figure 3c) images of WSe_{2-x} display the well-defined 2D morphology with the lateral size of ~800 nm, similar to those of WSe_2 (Figure S15). The element mapping images (Figure 3d) reveal the uniform distribution of W and Se elements in WSe_{2-x}. The high-resolution TEM (HRTEM, Figure 3e) image of WSe_2 unveils the distinct lattice fringes with a *d*-spacing of 0.28 nm, assigned to the (100) facet of WSe_2. The 3D topographic atom imaging profile (Figure 3f) of WSe_2 and corresponding lattice line scanning analysis (Figure 3g) reveal the well-resolved periodically arranged lattice atoms on WSe_2, indicating the highly crystalline structure of WSe_2. In parallel comparisons, WSe_{2-x} presents some disordered lattice regions (Figure 3h,i) with the loss of many lattice atoms (dotted circles, Figure 3j), suggesting the formation of abundant vacancies on WSe_{2-x}. The inductively coupled plasma analysis reveals a much reduced Se/W molar ratio of 1.79 relative to the WSe_2 nominal ratio (2), indicating the Se-deficient nature of WSe_{2-x}.

In the X-ray photoelectron spectroscopy (XPS, Figure 4a,b) spectra, the W 4f and Se 3d spectra of WSe_{2-x} are distinctly shifted to the lower binding energies compared to those of WSe_2, suggesting the decreased valence states of WSe_{2-x} derived from Se vacancies.[23] Compared to the featureless electron paramagnetic resonance (EPR, Figure 4c) spectra of WSe_2, WSe_{2-x} shows a strong EPR signal, confirming the enriched Se vacancies involved in WSe_{2-x}.[51] The coordination structures of WSe_2 and WSe_{2-x} are further investigated by the X-ray absorption near-edge structure (XANES) and extended X-ray absorption fine structure (EXAFS). The W L_3-edge XANES spectra (Figure 4d) show that WSe_{2-x} presents a low-E shift compared to WSe_2 and WO_2, suggesting the lower valence state of W ($\delta < 4$) of WSe_{2-x}, attributed to the electron donation from electron-rich Se vacancies.[53] The corresponding EXAFS spectra (Figure 4e) show that, compared to WSe_2

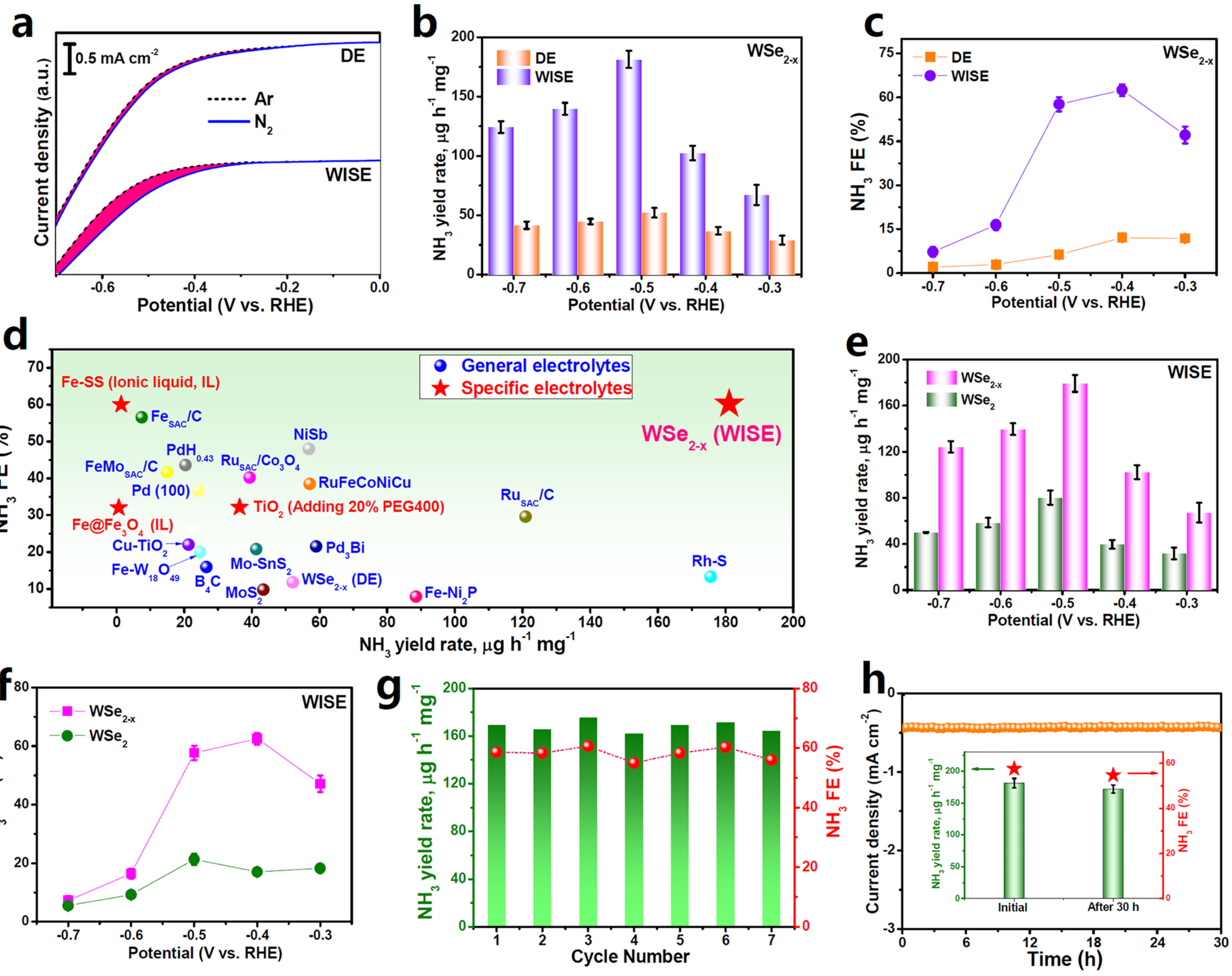

Figure 5. (a) LSV curves of WSe_{2-x} in Ar- and N_2-saturated DE (0.5 m $LiClO_4$) and WISE (12 m $LiClO_4$). (b,c) Comparison of (b) NH_3 yield rates and (c) FEs over WSe_{2-x} in DEs and WISEs at various potentials. (d) Comparison of the NRR performance for the state-of-the-art NRR electrocatalysts in general and specific electrolytes at ambient conditions. Comparison of (e) NH_3 yield rates and (f) FEs of WSe_2 and WSe_{2-x} in WISEs at various potentials. (g) Cycling test in WISE at −0.5 V. (h) Chronoamperometry test in WISEs at −0.5 V for 30 h (inset: NH_3 yields of initial and post-NRR electrolysis at −0.5 V).

(2.21 Å), WSe_{2-x} exhibits an elongated W−Se bond (2.25 Å) accompanied by a reduced bond intensity (Figure S16a). The W−Se bond elongation state of WSe_{2-x} can also be revealed by the wavelet transform (WT, Figure 4f) profiles in *k*-space (8.8 Å^{-1} for WSe_{2-x} and 8.5 Å^{-1} for WSe_2, Figure 2f), indicating the Se-vacancy-induced structure distortion. The EXAFS fitting results (Figure S16b and Table S1) show the coordination number of the W−Se shell being 5.38 and 5.96 for WSe_{2-x} and WSe_2, respectively, demonstrating the coordination-unsaturated W−Se bond structure of WSe_{2-x} caused by the Se vacancies. Meanwhile, the intensity maxima in the WT profiles (Figure 4f) display only W−Se without the existence of W−W and W−O coordination paths, proving the high purity of WSe_2 and WSe_{2-x}. Likewise, the information derived from Se K-edge XANES (Figure 4g), EXAFS (Figure 4h), and WT (Figure 4i) profiles follows trends similar to those obtained from the above W L_3-edge analyses. All of these characterizations confirm the successful preparation of Se-vacancy-rich WSe_{2-x}.

Electrochemical NRR measurements are performed in N_2-saturated $LiClO_4$ electrolytes using an H-type electrolytic cell.[23] All feeding gases are purified through an acid trap (0.05 M H_2SO_4) and an alkaline trap (0.1 M KOH) to remove any possible NH_3/NO_x contaminants (Figure S17). Prior to NRR tests, the combined colorimetric and ^{1}H nuclear magnetic resonance (NMR) experiments are carried out to verify the source of produced NH_3.[54−56] First, no NH_3 can be detected in any control colorimetric tests (Figure S18). In addition, $^{15}N_2$ isotopic labeling of the ^{1}H NMR spectrum (Figure S19) shows characteristic doublet coupling peaks matching well with the doublets of the $^{15}NH_4^+$ standard sample, confirming the $^{15}NH_4^+$ products derived from the NRR fed by $^{15}N_2$.[17] Additionally, the quantitative ^{1}H NMR measurement shows a similar result with that obtained by the indophenol method (Figure S20).[57] All of these experiments exclude the possible interference from any NH_3 contaminants and render reliable NRR measurements.

Figure 5a shows the linear sweep voltammetry (LSV) curves of WSe_{2-x} in Ar- and N_2-saturated DE (0.5 m $LiClO_4$) and WISE (12 m $LiClO_4$). The current density difference between Ar and N_2 in WISEs is much larger than that in DEs, indicating that the HER can be effectively suppressed in WISEs to enable potentially high NRR activity and selectivity. We then quantify

https://doi.org/10.1021/acsnano.2c00596

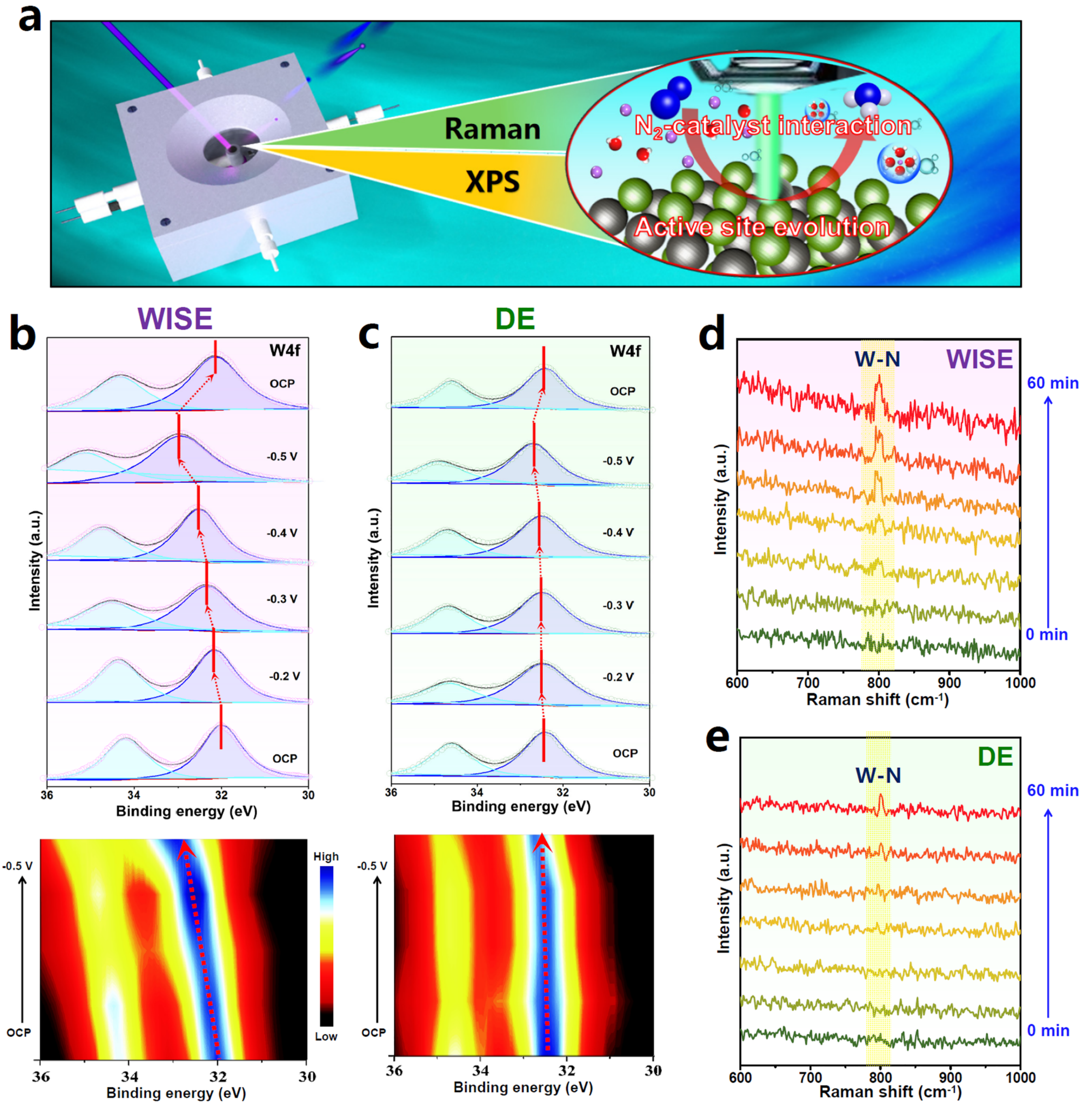

Figure 6. (a) Schematic of in situ XPS and Raman measurements. (b,c) In situ XPS W 4f spectra (top) and corresponding contour maps (bottom) of WSe_{2-x} during the NRR electrolysis at different potentials in DEs and WISEs. (d,e) In situ Raman spectra of WSe_{2-x} during the NRR electrolysis on WSe_{2-x} at various times in WISEs and DEs.

the NRR performance of WSe_{2-x} in different electrolytes by chronoamperometry at various potentials for 2 h, with produced NH_3 and possible N_2H_4 detected by UV−vis spectrophotometry.[58−60] No N_2H_4 is detected after NRR electrolysis in both DE and WISE (Figure S21). The calculated NH_3 yields and FEs of WSe_{2-x} in WISEs and DEs as a function of applied potential are plotted in Figure 5b,c (Figures S22 and S23), showing that the NH_3 yield in WISEs reaches a maximum of 181.3 μg h^{-1} mg^{-1} at −0.5 V, along with the highest FE of 62.5% at −0.4 V, which are 3.5 and 5.3 times higher than those in DE (52.1 μg h^{-1} mg^{-1}, 11.8%). Such excellent NRR performance enabled by WSe_{2-x} in WISEs outperforms nearly all of the current state-of-the-art NRR catalyst systems (Figure 5d and Table S2), demonstrating the superiority of WISEs in substantially boosting the NRR activity and selectivity. We also assess the NRR performance of Se-vacancy-free WSe_2 in WISEs (Figure 5e,f and Figure S24), which exhibits a much worse NRR activity with the optimum NH_3 yield (80.2 μg h^{-1} mg^{-1}) and FE (21.3%), 2.3 and 2.9 times lower than those of WSe_{2-x} in WISEs, respectively. A similar trend is also found in DE (Figures S25 and S26). This suggests that the catalyst engineering is equally important to attain the high NRR performance. The enhanced intrinsic NRR activity of WSe_{2-x} can be attributed to the Se-vacancy-induced synergetic effects of improved N_2 adsorption/protonation (Figure 1 and Figure S27), increased electrochemical active surface area (Figure S28), as well as accelerated electron transport kinetics (Figures S6 and S29).

In addition to the excellent NRR activity and selectivity, WSe_{2-x} also presents outstanding electrochemical stability in WISEs. A small variation in NH_3 yields/FEs is obtained upon seven successive cycles of NRR electrolysis (Figure 5g), proving the good cycling stability. The chronoamperometry test for 30 h continuous NRR electrolysis shows a steady current density (Figure 5h), and the resulting NH_3 yield and FE decrease slightly relative to the initial one (Figure 5h, inset),[61] affirming the excellent long-term durability. After stability tests, WSe_{2-x} well retains its original morphology (Figure S30), crystal phase (Figure S31), and chemical structures (Figure S32), validating the good structural durability.

To gain further insights into the exceptional NRR performance of WSe_{2-x} in WISE, in situ XPS and Raman measurements are carried out (Figure 6a). First, in situ XPS measurements are performed to investigate the dynamic change in electronic states of the active sites in different electrolytes during the NRR process. Based on the above DFT calculations (Figure S2), the Se-vacancy-induced W−W−W trimers are determined to be the active sites for the NRR. Accordingly, the XPS W 4f spectra of WSe_{2-x} operated at different potentials in DE and WISE are collected and displayed in Figure 6b,c. In WISEs (Figure 6b), with increasing the potential from OCP to −0.5 V, the W 4f spectra of WSe_{2-x} progressively shift to a higher binding energy, suggesting the effective N_2 activation process where W−W−W active sites on WSe_{2-x} back-donate numerous electrons into the adsorbed N_2, leading to the increased valence state of W. Noticeably, a dramatic W 4f shift can be observed at −0.5 V, which means the most intense NRR occurs in this potential, consistent with the NRR measurements (Figure 5b). In DE (Figure 6c), however, the W 4f position remains almost unchanged from OCP to 0.4 V and shows a slight high-E shift at −0.5 V, implying the small variation in electronic state of WSe_{2-x} during the NRR process. In this scenario, WSe_{2-x} provides very limited electrons participating in the N_2 activation process, thus resulting in a poor NRR activity in DE. These in situ XPS results demonstrate that WISE can promote the π-back-donation ability of W active sites to favorably transfer the electrons into the antibonding orbitals of N_2 molecules for enhancing the N_2 activation.[62] Note that when the applied potential is set back to OCP, the electronic states of W 4f spectra can reverse back to the initial states in both DEs and WISEs (Figure 6b,c), indicating the reversibility of W active sites in the NRR cycle and also confirming the high electrocatalytic stability of WSe_{2-x} in WISEs, in accordance with the stability measurements (Figure 5g,h).

The N_2−catalyst interactions in different electrolytes are further investigated by in situ Raman measurements (Figure 6d,e and Figure S33). During the NRR process in WISEs (Figure 6d), a prominent peak related to W−N stretching vibration appears in the Raman spectra of ~800 cm^{-1}, and the peak intensity continually enhances with increasing reaction time, suggesting that WISEs render the considerable adsorption of N species on WSe_{2-x} where the W−W−W active sites chemically bond with the absorbed N_2 to weaken and dissociate the N≡N bond, resulting in boosted N_2 activation and high NRR activity. In sharp contrast, the Raman spectra in DEs (Figure 6e) display a rather weak W−N vibration band in the whole NRR reaction process, indicating that WSe_{2-x} cannot effectively stabilize and activate N_2 in DE, causing insufficient N_2 dissociation and poor NRR activity. These in situ XPS and Raman findings corroborate that, in addition to suppressed HER and improved N_2 affinity, WISEs can also promote the π-back-donation ability of active sites to enhance the N_2 activation and facilitate the NRR activity.

CONCLUSIONS

In summary, both high NRR activity and selectivity (118.3 μg h^{-1} mg^{-1}, 62.5%) were realized over WSe_{2-x} in WISEs (12 M $LiClO_4$), attributed to the pivotal role of WISEs in suppressing the HER, improving the N_2 affinity on the catalyst surface, and boosting the π-back-donation ability of active sites. This work not only deepens the understanding of NRR mechanisms in WISEs but also demonstrates the great potential for the combination of catalyst and electrolyte engineering toward exceptional N_2 electroreduction and beyond.

EXPERIMENTAL SECTION

Materials. Bulk WSe_2 powder (>99.5 wt %) was purchased from Guangzhou Nano Chemical Technology Co., Ltd. $C_4H_4O_6KNa\cdot 4H_2O$ (≥99.9 wt %), $C_5FeN_6Na_2O$ (≥99.0%), $SO_2(NH_2)_2$ (≥99.5%), NH_4Cl (≥99.5%), N_2H_4 (≥99.0%), $C_7H_6O_3$ (≥99.5%), $C_7H_5NaO_3$ (≥99.5%), $LiClO_4$ (≥99.9%), $C_{12}H_{14}N_2\cdot 2HCl$ (≥99.0%), NaClO (≥99.9 wt %), $C_9H_{11}NO$ (≥99.5%), D_2O (≥99.9%), DMSO (≥99.0%), and Nafion (5 wt %) were provided from Sigma-Aldrich Chemical Reagent Co., Ltd. and Sinopharm Chemical Reagent Co., Ltd. N_2 (≥99.999%) and Ar (≥99.999%) were provided from Lanzhou Xinwanke, Co., Ltd. All of the reagents were of analytical grade and were used as received without further purification.

Synthesis of WSe_2 and WSe_{2-x} Nanosheets. All of the chemicals are of analytical grade and used as received. Typically, 200 mg of bulk WSe_2 powders (99.5%) was ground using an agate mortar with the addition of 2 mL of NMP for 2 h. Then the as-ground powders were subjected to liquid exfoliation by ultrasonication in anhydrous ethanol for 10 h. The precipitates were collected via centrifugation, further washed with deionized water and ethanol several times, and dried at 60 °C overnight, obtaining WSe_2 nanosheets. Afterward, WSe_2 nanosheets were transferred into a tube furnace and annealed at 500 °C in flowing 5% H_2/Ar atmosphere for 2 h, obtaining WSe_{2-x} nanosheets.

Calculation Details. Cambridge sequential total energy package (CASTEP) was used for all DFT calculations. Perdew−Burke−Ernzerhof (PBE) generalized gradient approximation (GGA) functional was used to model the exchange-correlation interactions. DFT-D method was employed to calculate the van der Waals interaction. Molecular dynamics simulations were carried out using a force field type of COMPASS II, and the MD simulations were performed under the universal field with the total simulation time of 5 ns at a time step of 1 fs.

Electrochemical Experiments. Electrochemical measurements were carried out at ambient conditions on a CHI-760E electrochemical workstation. All potentials were referenced to reversible hydrogen electrode (RHE) by E_{RHE} (V) = $E_{Ag/AgCl}$ + 0.197 + 0.059 × pH. The NRR measurements were carried out in an H-type two-compartment electrochemical cell separated by a Nafion 211 membrane, and a flow of N_2 (99.999%, 20 mL min^{-1}) was continuously fed to the cathodic compartment during the potentiostatic testing. After NRR electrolysis at each potentials for 2 h, the produced NH_3 was quantitatively determined by the indophenol blue method.

Characterizations. SEM was performed on a ZEISS GeminiSEM-500 microscope. TEM, HRTEM, and high-angle annular dark-field scanning transmission electron microscopy were conducted on a Tecnai G^2 F20 microscope. An XRD pattern was obtained with a Rigaku D/max 2400 diffractometer. Ex situ XPS analysis was carried out on a PHI 5702 spectrometer. EPR measurements were taken on a

Bruker ESP-300 spectrometer. Dinitrogen temperature-programmed desorption (N_2-TPD) profiles were collected on a Chem-BET 3000 apparatus. NMR measurement was performed on a Bruker superconducting magnet NMR spectrometer (500 MHz). In situ XPS measurements were performed on a Thermo ESCALAB 250Xi spectrometer using a tailor-made X-ray cell consisting of an analysis chamber, a reaction chamber, and a preparation chamber. During the XPS potentiostatic testing, the catalyst was first placed into a reaction chamber in an electrolyte (saturated with N_2), and then the reactor was then vacuumized and transferred to the analysis chamber. The XPS signals were collected at various applied potentials with a scan rate of 2 mV s^{-1}. In situ Raman measurements were performed on a confocal Raman spectrometer (Horiba HR-800, 532 nm) using a tailor-made electrolytic cell, and the Raman spectra were recorded at different electrolysis times of 0−60 min under the applied potential of −0.5 V (RHE).

ASSOCIATED CONTENT

Supporting Information

The Supporting Information is available free of charge at https://pubs.acs.org/doi/10.1021/acsnano.2c00596.

> Description of calculation and experiment details, DFT results for differential charge density and free energy diagrams of WSe_2 and WSe_{2-x}, ESP diagrams of Li−H_2O interactions, MD results for the snapshots of different electrolyte systems and corresponding RDF curves, SEM/TEM images of WSe_2, EXAFS fitting results, N-source determination experiments, NH_3 calibration curves in DE and WISE, chronoamperometry/UV−vis data for calculating NH_3 yields and FEs in various catalyst systems, SEM/TEM/XRD/XPS characterizations of WSe_{2-x} after stability test in WISE (PDF)

AUTHOR INFORMATION

Corresponding Author

Ke Chu − *School of Materials Science and Engineering, Lanzhou Jiaotong University, Lanzhou 730070, China;* orcid.org/0000-0002-0606-2689; Email: chuk630@mail.lzjtu.cn

Authors

Peng Shen − *School of Materials Science and Engineering, Lanzhou Jiaotong University, Lanzhou 730070, China*

Xingchuan Li − *School of Materials Science and Engineering, Lanzhou Jiaotong University, Lanzhou 730070, China*

Yaojing Luo − *School of Materials Science and Engineering, Lanzhou Jiaotong University, Lanzhou 730070, China*

Yali Guo − *School of Materials Science and Engineering, Lanzhou Jiaotong University, Lanzhou 730070, China*

Xiaolin Zhao − *National Engineering Laboratory for Electric Vehicles, Beijing Institute of Technology, Beijing 100081, China*

Complete contact information is available at: https://pubs.acs.org/10.1021/acsnano.2c00596

Author Contributions

P.S. performed the computations and wrote the original draft. X.L. and Y.L. prepared and characterized the catalysts. Y.L. and Y.G. conducted the electrochemical measurements. Y.G. and X.Z. performed in situ XPS/Raman measurements. K.C. directed the overall research and supervised the project. All authors contributed to discussing the paper.

Notes

The authors declare no competing financial interest.

ACKNOWLEDGMENTS

This work is supported by the National Natural Science Foundation of China (52161025) and Natural Science Foundation of Gansu Province (20JR10RA241).

REFERENCES

(1) Howard, J. B.; Rees, D. C. Structural Basis of Biological Nitrogen Fixation. *Chem. Rev.* **1996**, *96*, 2965−2982.

(2) van Breemen, N. Nitrogen Cycle-Natural Organic Tendency. *Nature* **2002**, *415*, 381−382.

(3) Ren, Y.; Yu, C.; Tan, X.; Huang, H.; Wei, Q.; Qiu, J. Strategies to Suppress Hydrogen Evolution for Highly Selective Electrocatalytic Nitrogen Reduction: Challenges and Perspectives. *Energy Environ. Sci.* **2021**, *14*, 1176−1193.

(4) Li, Y.; Wang, H.; Priest, C.; Li, S.; Xu, P.; Wu, G. Advanced Electrocatalysis for Energy and Environmental Sustainability via Water and Nitrogen Reactions. *Adv. Mater.* **2021**, *33*, 2000381.

(5) Qing, G.; Ghazfar, R.; Jackowski, S. T.; Habibzadeh, F.; Ashtiani, M. M.; Chen, C.-P.; Smith, M. R.; Hamann, T. W. Recent Advances and Challenges of Electrocatalytic N_2 Reduction to Ammonia. *Chem. Rev.* **2020**, *120*, 5437−5516.

(6) Wang, T.; Liu, Q.; Li, T.; Lu, S.; Chen, G.; Shi, X.; Asiri, A. M.; Luo, Y.; Ma, D.; Sun, X. A Magnetron Sputtered Mo_3Si Thin Film: An Efficient Electrocatalyst for N_2 Reduction under Ambient Conditions. *J. Mater. Chem. A* **2021**, *9*, 884−888.

(7) Wang, T.; Li, S.; He, B.; Zhu, X.; Luo, Y.; Liu, Q.; Li, T.; Lu, S.; Ye, C.; Asiri, A. M.; Sun, X. Commercial Indium-Tin Oxide Glass: A Catalyst Electrode for Efficient N_2 Reduction at Ambient Conditions. *Chin. J. Catal.* **2021**, *42*, 1024−1029.

(8) Du, Z.; Liang, J.; Li, S.; Xu, Z.; Li, T.; Liu, Q.; Luo, Y.; Zhang, F.; Liu, Y.; Kong, Q.; Shi, X.; Tang, B.; Asiri, A. M.; Li, B.; Sun, X. Alkylthiol Surface Engineering: An Effective Strategy toward Enhanced Electrocatalytic N_2-to-NH_3 Fixation by a CoP Nanoarray. *J. Mater. Chem. A* **2021**, *9*, 13861−13866.

(9) Cheng, X.; Wang, J.; Xiong, W.; Wang, T.; Wu, T.; Lu, S.; Chen, G.; Gao, S.; Shi, X.; Jiang, Z.; Niu, X.; Sun, X. Greatly Enhanced Electrocatalytic N_2 Reduction over V_2O_3/C by P Doping. *ChemNanoMat* **2020**, *6*, 1315−1319.

(10) Shen, H.; Choi, C.; Masa, J.; Li, X.; Qiu, J.; Jung, Y.; Sun, Z. Electrochemical Ammonia Synthesis: Mechanistic Understanding and Catalyst Design. *Chem.* **2021**, *7*, 1708−1754.

(11) Zheng, J.; Lyu, Y.; Qiao, M.; Veder, J. P.; Marco, R. D.; Bradley, J.; Wang, R.; Li, Y.; Huang, A.; Jiang, S. P.; Wang, S. Tuning the Electron Localization of Gold Enables the Control of Nitrogen-to-Ammonia Fixation. *Angew. Chem., Int. Ed.* **2019**, *58*, 18604−18609.

(12) Xue, Z.-H.; Zhang, S.-N.; Lin, Y.-X.; Su, H.; Zhai, G.-Y.; Han, J.-T.; Yu, Q.-Y.; Li, X.-H.; Antonietti, M.; Chen, J.-S. Electrochemical Reduction of N_2 into NH_3 by Donor−Acceptor Couples of Ni and Au Nanoparticles with a 67.8% Faradaic Efficiency. *J. Am. Chem. Soc.* **2019**, *141*, 14976−14980.

(13) Wang, J.; Yu, L.; Hu, L.; Chen, G.; Xin, H.; Feng, X. Ambient Ammonia Synthesis via Palladium-Catalyzed Electrohydrogenation of Dinitrogen at Low Overpotential. *Nat. Commun.* **2018**, *9*, 1795.

(14) Jin, H.; Li, L.; Liu, X.; Tang, C.; Xu, W.; Chen, S.; Song, L.; Zheng, Y.; Qiao, S.-Z. Nitrogen Vacancies on 2D Layered W_2N_3: A Stable and Efficient Active Site for Nitrogen Reduction Reaction. *Adv. Mater.* **2019**, *31*, 1902709.

(15) Zhang, L.; Ji, X.; Ren, X.; Ma, Y.; Shi, X.; Tian, Z.; Asiri, A. M.; Chen, L.; Tang, B.; Sun, X. Electrochemical Ammonia Synthesis via Nitrogen Reduction Reaction on a MoS_2 Catalyst: Theoretical and Experimental Studies. *Adv. Mater.* **2018**, *30*, 1800191.

(16) Zhang, Y.; Qiu, W.; Ma, Y.; Luo, Y.; Tian, Z.; Cui, G.; Xie, F.; Chen, L.; Li, T.; Sun, X. High-Performance Electrohydrogenation of N_2 to NH_3 Catalyzed by Multishelled Hollow Cr_2O_3 Microspheres under Ambient Conditions. *ACS Catal.* **2018**, *8*, 8540−8544.

(17) Zhang, L. L.; Ding, L. X.; Chen, G. F.; Yang, X. F.; Wang, H. H. Ammonia Synthesis under Ambient Conditions: Selective Electro-

reduction of Dinitrogen to Ammonia on Black Phosphorus Nanosheets. *Angew. Chem., Int. Ed.* **2019**, *131*, 2638−2642.

(18) Liu, S.; Wang, M.; Qian, T.; Ji, H.; Liu, J.; Yan, C. Facilitating Nitrogen Accessibility to Boron-Rich Covalent Organic Frameworks via Electrochemical Excitation for Efficient Nitrogen Fixation. *Nat. Commun.* **2019**, *10*, 3898.

(19) Qiu, W.; Xie, X.-Y.; Qiu, J.; Fang, W.-H.; Liang, R.; Ren, X.; Ji, X.; Cui, G.; Asiri, A. M.; Cui, G.; Tang, B.; Sun, X. High-Performance Artificial Nitrogen Fixation at Ambient Conditions Using a Metal-Free Electrocatalyst. *Nat. Commun.* **2018**, *9*, 3485.

(20) Zhang, M.; Choi, C.; Huo, R.; Gu, G. H.; Hong, S.; Yan, C.; Xu, S.; Robertson, A. W.; Qiu, J.; Jung, Y.; Sun, Z. Reduced Graphene Oxides with Engineered Defects Enable Efficient Electrochemical Reduction of Dinitrogen to Ammonia in Wide Ph Range. *Nano Energy* **2020**, *68*, 104323.

(21) Sun, Z.; Huo, R.; Choi, C.; Hong, S.; Wu, T.-S.; Qiu, J.; Yan, C.; Han, Z.; Liu, Y.; Soo, Y.-L.; Jung, Y. Oxygen Vacancy Enables Electrochemical N_2 Fixation over WO_3 with Tailored Structure. *Nano Energy* **2019**, *62*, 869−875.

(22) Han, Z.; Choi, C.; Hong, S.; Wu, T.-S.; Soo, Y.-L.; Jung, Y.; Qiu, J.; Sun, Z. Activated TiO_2 with Tuned Vacancy for Efficient Electrochemical Nitrogen Reduction. *Appl. Catal., B* **2019**, *257*, 117896.

(23) Chu, K.; Wang, J.; Liu, Y. P.; Li, Q. Q.; Guo, Y. L. Mo-Doped SnS_2 with Rich S-Vacancies for Highly Efficient Electrocatalytic N_2 Reduction: The Critical Role of Mo-Sn-Sn Trimer. *J. Mater. Chem. A* **2020**, *8*, 7117−7124.

(24) Li, Q.; Guo, Y.; Tian, Y.; Liu, W.; Chu, K. Activating VS_2 Basal Planes for Enhanced NRR Electrocatalysis: The Synergistic Role of S-Vacancies and B Dopants. *J. Mater. Chem. A* **2020**, *8*, 16195−16202.

(25) Luo, Y.; Li, Q.; Tian, Y.; Liu, Y.; Chu, K. Amorphization Engineered VSe_{2-x} Nanosheets with Abundant Se-Vacancies for Enhanced N_2 Electroreduction. *J. Mater. Chem. A* **2022**, *10*, 1742−1749.

(26) Chu, K.; Li, X.; Li, Q.; Guo, Y.; Zhang, H. Synergistic Enhancement of Electrocatalytic Nitrogen Reduction over Boron Nitride Quantum Dots Decorated Nb_2CT_x-Mxene. *Small* **2021**, *17*, 2102363.

(27) Chu, K.; Cheng, Y.; Li, Q.; Liu, Y.; Tian, Y. Fe-Doping Induced Morphological Changes, Oxygen Vacancies and Ce^{3+}−Ce^{3+} Pairs in CeO_2 for Promoting Electrocatalytic Nitrogen Fixation. *J. Mater. Chem. A* **2020**, *8*, 5865−5873.

(28) Chu, K.; Liu, Y.-p.; Cheng, Y.-h.; Li, Q.-q. Synergistic Boron-Dopants and Boron-Induce Oxygen Vacancies in MnO_2 Nanosheets to Promote Electrocatalytic Nitrogen Reduction. *J. Mater. Chem. A* **2020**, *8*, 5200−5208.

(29) Chu, K.; Luo, Y.; Shen, P.; Li, X.; Li, Q.; Guo, Y. Unveiling the Synergy of O-Vacancy and Heterostructure over MoO_{3-x}/MXene for N_2 Electroreduction to NH_3. *Adv. Energy. Mater.* **2022**, *12*, 2103022.

(30) Li, Q.; Shen, P.; Tian, Y.; Li, X.; Chu, K. Metal-Free BN Quantum Dots/Graphitic C_3N_4 Heterostructure for Nitrogen Reduction Reaction. *J. Colloid Interface Sci.* **2022**, *606*, 204−212.

(31) Li, X.; Luo, Y.; Li, Q.; Guo, Y.; Chu, K. Constructing an Electron-Rich Interface over an Sb/Nb_2CT_x−MXene Heterojunction for Enhanced Electrocatalytic Nitrogen Reduction. *J. Mater. Chem. A* **2021**, *9*, 15955−15962.

(32) Guo, W.; Zhang, K.; Liang, Z.; Zou, R.; Xu, Q. Electrochemical Nitrogen Fixation and Utilization: Theories, Advanced Catalyst Materials and System Design. *Chem. Soc. Rev.* **2019**, *48*, 5658−5716.

(33) Chen, G. F.; Ren, S. Y.; Zhang, L. L.; Cheng, H.; Luo, Y. R.; Zhu, K. H.; Ding, L. X.; Wang, H. H. Advances in Electrocatalytic N_2 Reduction-Strategies to Tackle the Selectivity Challenge. *Small Methods* **2019**, *3*, 1800337.

(34) Guo, C.; Ran, J.; Vasileff, A.; Qiao, S.-Z. Rational Design of Electrocatalysts and Photo (Electro) Catalysts for Nitrogen Reduction to Ammonia (NH_3) under Ambient Conditions. *Energy Environ. Sci.* **2018**, *11*, 45−56.

(35) Guang, H.-L.; Zhu, S.-L.; Liang, Y.-Q.; Wu, S.-L.; Li, Z.-Y.; Luo, S.-Y.; Cui, Z.-D.; Inoue, A. Highly Efficient Nanoporous CoBP Electrocatalyst for Hydrogen Evolution Reaction. *Rare Metals* **2021**, *40*, 1031−1039.

(36) Liu, J.-D.; Wei, Z.-X.; Dou, Y.-H.; Feng, Y.-Z.; Ma, J.-M. Ru-Doped Phosphorene for Electrochemical Ammonia Synthesis. *Rare Metals* **2020**, *39*, 874−880.

(37) Wei, Z.-X.; Zhu, Y.-T.; Liu, J.-Y.; Zhang, Z.-C.; Hu, W.-P.; Xu, H.; Feng, Y.-Z.; Ma, J.-M. Recent Advance in Single-Atom Catalysis. *Rare Metals* **2021**, *40*, 767−789.

(38) Suryanto, B. H.; Kang, C. S.; Wang, D.; Xiao, C.; Zhou, F.; Azofra, L. M.; Cavallo, L.; Zhang, X.; MacFarlane, D. R. Rational Electrode−Electrolyte Design for Efficient Ammonia Electrosynthesis under Ambient Conditions. *ACS Energy Lett.* **2018**, *3*, 1219−1224.

(39) Zhou, F.; Azofra, L. M.; Ali, M.; Kar, M.; Simonov, A. N.; McDonnell-Worth, C.; Sun, C.; Zhang, X.; MacFarlane, D. R. Electro-Synthesis of Ammonia from Nitrogen at Ambient Temperature and Pressure in Ionic Liquids. *Energy Environ. Sci.* **2017**, *10*, 2516−2520.

(40) Guo, Y.; Gu, J.; Zhang, R.; Zhang, S.; Li, Z.; Zhao, Y.; Huang, Z.; Fan, J.; Chen, Z.; Zhi, C. Molecular Crowding Effect in Aqueous Electrolytes to Suppress Hydrogen Reduction Reaction and Enhance Electrochemical Nitrogen Reduction. *Adv. Energy. Mater.* **2021**, *11*, 2101699.

(41) Liang, T.; Hou, R.; Dou, Q.; Zhang, H.; Yan, X. The Applications of Water-in-Salt Electrolytes in Electrochemical Energy Storage Devices. *Adv. Funct. Mater.* **2021**, *31*, 2006749.

(42) Sui, Y.; Ji, X. Anticatalytic Strategies to Suppress Water Electrolysis in Aqueous Batteries. *Chem. Rev.* **2021**, *121*, 6654−6695.

(43) Dubouis, N.; Lemaire, P.; Mirvaux, B.; Salager, E.; Deschamps, M.; Grimaud, A. The Role of the Hydrogen Evolution Reaction in the Solid−Electrolyte Interphase Formation Mechanism for "Water-in-Salt" Electrolytes. *Energy Environ. Sci.* **2018**, *11*, 3491−3499.

(44) Wang, M.; Liu, S.; Ji, H.; Yang, T.; Qian, T.; Yan, C. Salting-out Effect Promoting Highly Efficient Ambient Ammonia Synthesis. *Nat. Commun.* **2021**, *12*, 3198.

(45) Ling, C.; Niu, X.; Li, Q.; Du, A.; Wang, J. Metal-Free Single Atom Catalyst for N_2 Fixation Driven by Visible Light. *J. Am. Chem. Soc.* **2018**, *140*, 14161−14168.

(46) Zhao, J.; Chen, Z. Single Mo Atom Supported on Defective Boron Nitride Monolayer as an Efficient Electrocatalyst for Nitrogen Fixation: A Computational Study. *J. Am. Chem. Soc.* **2017**, *139*, 12480−12487.

(47) Chu, K.; Liu, Y.; Li, Y.; Wang, J.; Zhang, H. Electronically Coupled SnO_2 Quantum Dots and Graphene for Efficient Nitrogen Reduction Reaction. *ACS Appl. Mater. Interfaces* **2019**, *11*, 31806−31815.

(48) Li, Y.; Zhang, Q.; Li, C.; Fan, H.-N.; Luo, W.-B.; Liu, H.-K.; Dou, S.-X. Atomically Dispersed Metal Dimer Species with Selective Catalytic Activity for Nitrogen Electrochemical Reduction. *J. Mater. Chem. A* **2019**, *7*, 22242−22247.

(49) Song, Y.; Johnson, D.; Peng, R.; Hensley, D. K.; Bonnesen, P. V.; Liang, L.; Huang, J.; Yang, F.; Zhang, F.; Qiao, R.; et al. A Physical Catalyst for the Electrolysis of Nitrogen to Ammonia. *Sci. Adv.* **2018**, *4*, e1700336.

(50) Wu, T.; Xing, Z.; Mou, S.; Li, C.; Qiao, Y.; Liu, Q.; Zhu, X.; Luo, Y.; Shi, X.; Zhang, Y.; Sun, X. Greatly Improving Electrochemical N_2 Reduction over TiO_2 Nanoparticle by Fe Doping. *Angew. Chem., Int. Ed.* **2019**, *58*, 18449−18453.

(51) Chu, K.; Nan, H.; Li, Q.; Guo, Y.; Tian, Y.; Liu, W. Amorphous MoS_3 Enriched with Sulfur Vacancies for Efficient Electrocatalytic Nitrogen Reduction. *J. Energy Chem.* **2021**, *53*, 132−138.

(52) Wang, M.; Liu, S.; Ji, H.; Yang, T.; Qian, T.; Yan, C. Salting-out Effect Promoting Highly Efficient Ambient Ammonia Synthesis. *Nat. Commun.* **2021**, *12*, 3198.

(53) Jia, C.; Tan, X.; Zhao, Y.; Ren, W.; Li, Y.; Su, Z.; Smith, S. C.; Zhao, C. Sulfur-Dopant-Promoted Electroreduction of CO_2 over Coordinatively Unsaturated Ni-N_2 Moieties. *Angew. Chem., Int. Ed.* **2021**, *60*, 23342−23348.

(54) Tang, C.; Qiao, S.-Z. How to Explore Ambient Electrocatalytic Nitrogen Reduction Reliably and Insightfully. *Chem. Soc. Rev.* **2019**, *48*, 3166−3180.

(55) Suryanto, B. H. R.; Du, H.-L.; Wang, D.; Chen, J.; Simonov, A. N.; MacFarlane, D. R. Challenges and Prospects in the Catalysis of Electroreduction of Nitrogen to Ammonia. *Nat. Catal.* **2019**, *2*, 290−296.

(56) Andersen, S. Z.; Čolić, V.; Yang, S.; Schwalbe, J. A.; Nielander, A. C.; McEnaney, J. M.; Enemark-Rasmussen, K.; Baker, J. G.; Singh, A. R.; Rohr, B. A.; Statt, M. J.; Blair, S. J.; Mezzavilla, S.; Kibsgaard, J.; Vesborg, P. C. K.; Cargnello, M.; Bent, S. F.; Jaramillo, T. F.; Stephens, I. E. L.; Nørskov, J. K.; Chorkendorff, I. A Rigorous Electrochemical Ammonia Synthesis Protocol with Quantitative Isotope Measurements. *Nature* **2019**, *570*, 504−508.

(57) Chu, K.; Liu, Y.; Li, Y.; Zhang, H.; Tian, Y. Efficient Electrocatalytic N_2 Reduction on CoO Quantum Dots. *J. Mater. Chem. A* **2019**, *7*, 4389−4394.

(58) Chu, K.; Liu, Y. P.; Li, Y. B.; Guo, Y. L.; Tian, Y. Two-Dimensional (2D)/2D Interface Engineering of MoS_2/C_3N_4 Heterostructure for Promoted Electrocatalytic Nitrogen Fixation. *ACS Appl. Mater. Interfaces* **2020**, *12*, 7081−7090.

(59) Gu, W.; Guo, Y.; Li, Q.; Tian, Y.; Chu, K. Lithium Iron Oxide ($LiFeO_2$) for Electroreduction of Dinitrogen to Ammonia. *ACS Appl. Mater. Interfaces* **2020**, *12*, 37258−37264.

(60) Li, X.; Tian, Y.; Wang, X.; Guo, Y.; Chu, K. $SnNb_2O_6$ Nanosheets for the Electrocatalytic NRR: Dual-Active-Center Mechanism of Nb_{3c} and Sn_{4c}−Nb_{5c} Dimer. *Sustain. Energy Fuels* **2021**, *5*, 4277−4283.

(61) Zhao, Z.; Park, J.; Choi, C.; Hong, S.; Hui, X.; Zhang, H.; Benedict Lo, T. W.; Robertson, A. W.; Lv, Z.; Jung, Y.; Sun, Z. Engineering Vacancy and Hydrophobicity of Two-Dimensional $TaTe_2$ for Efficient and Stable Electrocatalytic N_2 Reduction. *Innovation* **2022**, *3*, 100190.

(62) Yang, C.; Zhu, Y.; Liu, J.; Qin, Y.; Wang, H.; Liu, H.; Chen, Y.; Zhang, Z.; Hu, W. Defect Engineering for Electrochemical Nitrogen Reduction Reaction to Ammonia. *Nano Energy* **2020**, *77*, 105126.

https://doi.org/10.1021/acsnano.2c00596

Supporting Information

High-Efficiency N_2 Electroreduction Enabled by Se-Vacancy-Rich WSe_{2-x} in Water-in-Salt Electrolytes

Peng Shen [1], Xingchuan Li [1], Yaojing Luo [1], Yali Guo [1], Xiaolin Zhao [2], Ke Chu [1]*

[1]*School of Materials Science and Engineering, Lanzhou Jiaotong University, Lanzhou 730070, China*

[2]*National Engineering Laboratory for Electric Vehicles, Beijing Institute of Technology, Beijing 100081, Beijing, China*

*Corresponding author. E-mail address: chuk630@mail.lzjtu.cn (K. Chu)

Supplementary experimental

Calculation details

Spin-polarized DFT calculations were carried out using a Cambridge sequential total energy package (CASTEP). Perdew-Burke-Ernzerhof (PBE) generalized gradient approximation (GGA) functional was used to model the exchange-correlation interactions. DFT-D method was employed to calculate the van der Waals (vdW) interaction. The electron wave functions were expanded using plane waves with a cutoff energy of 400 eV, and a Monkhorst-Pack grid (4 × 4 × 1) was used for k-point sampling. The convergence of energy and forces were set to be 2×10^{-5} eV and 0.01 eV $Å^{-1}$. The electron wave functions were expanded using plane waves with a cutoff energy of 400 eV. WSe_2 (001) slab was modeled by a 4×4 supercell, and a vacuum space of around 15 Å was set along the z direction to avoid the interaction between periodical images.

The adsorption energy (ΔE) is defined as [1]

$$\Delta E = E_{\text{ads/slab}} - E_{\text{ads}} - E_{\text{slab}} \tag{1}$$

where $E_{\text{ads/slab}}$, E_{ads} and E_{slab} are the total energies for adsorbed species on slab, adsorbed species and isolated slab, respectively.

The Gibbs free energy (ΔG, 298 K) of reaction steps is calculated by [1]:

$$\Delta G = \Delta E + \Delta ZPE - T\Delta S \tag{2}$$

where ΔE is the adsorption energy, ΔZPE is the zero point energy difference and $T\Delta S$ is the entropy difference between the gas phase and adsorbed state. The entropies of free gases were acquired from the NIST database.

Molecular dynamics (MD) simulations were carried out using a force field type of COMPASS II. The non-bond interaction was processed by Ewald with accuracy of 10^{-4} Kcal/mol and the repulsive cutoff was chosen as 12 Å. The electrolyte systems were modeled by cubic cells with randomly filling 2000 H_2O, 100 N_2 molecules and a certain number of $LiClO_4$ for different concentrations of electrolytes (0.1-20 m). After geometry optimization, the MD simulations were performed under the universal field with the total simulation time of 5 ns at a time step of 1 fs.

The radial distribution function (RDF) is calculated as

$$g(r) = \frac{dN}{4\pi\rho r^2 dr} \tag{3}$$

where dN is the amount of particle N_2 in the shell between the central particle r and $r+dr$, ρ is the number density of N_2.

The mean square displacement (MSD) is calculated as

$$MSD = <|r(t) - r(0)|^2> \tag{4}$$

where $r(t)$ and $r(0)$ are the displacement of the particle at final and initial moments, respectively.

The diffusion coefficient (DC) is calculated as

$$DC = \lim_{t \to \infty} \frac{1}{6t} <|r(t) - r(0)|^2> \tag{5}$$

where t is the time it takes for the particle to diffuse.

Electrochemical experiments

Electrochemical measurements were performed under ambient conditions on a CHI-760E electrochemical workstation using Ag/AgCl (saturated KCl) as a reference electrode, graphite rod as a counter electrode, and as-prepared carbon cloth (CC) sample as working electrodes. To prepared working electrode, the as-received CC was pretreated by soaking it in 0.5 M H_2SO_4 for 12 h, and then washed with deionized water several times and dried at 60 ^oC for 24 h. Then 1 mg of the catalysts were dispersed in 100 μL of ethyl alcohol containing 5 μL of Nafion (5 wt%) under ultrasonication to form a homogeneous ink. Afterwards, 20 μL of well-dispersed catalysts were covered on the pretreated CC (0.2 mg cm^{-2}) and then dried for measurements. All potentials were referenced to reversible hydrogen electrode (RHE) by following equation: E_{RHE} (V)=$E_{Ag/AgCl}$+0.197+0.059×pH. The NRR measurements were carried out in an H-type two-compartment electrochemical cell separated by a Nafion 211 membrane. The Nafion membrane was pretreated by heating it in 5% H_2O_2 aqueous solution at 80 °C for 1 h and then in deionized water at 80 °C for another 1 h. Prior to NRR tests, all the feeding gases were purified through acid trap

(0.05 M H_2SO_4) and alkaline trap (0.1 M KOH)) to remove any possible contaminants (NH_3 and NO_x). A flow of N_2 (99.999%) with a rate of 20 mL min^{-1} was continuously fed to the cathodic compartment in the process of potentiostatic testing. After electrolysis at specified potentials for 2 h, the produced NH_3 was quantitatively determined by the indophenol blue method[2], and the possible byproduct (N_2H_4) was determined by the method of Watt and Chrisp[3]. The detailed procedures are provided by our previous publications [4-6].

Calculations of NH_3 yield and Faradaic efficiency

$$\mathrm{NH_3}\ \text{yield}\ (\mu\text{g h}^{-1}\ \text{mg}_{\text{cat.}}^{-1}) = \frac{c_{\mathrm{NH_3}} \times V}{t \times m} \tag{6}$$

Faradaic efficiency was calculated by the following equation:

$$\text{Faradaic efficiency (\%)} = \frac{3 \times F \times c_{\mathrm{NH_3}} \times V}{17 \times Q} \times 100\% \tag{7}$$

where c_{NH3} (μg mL^{-1}) is the measured NH_3 concentration, V (mL) is the volume of the electrolyte, t (h) is the reduction time and m (mg) is the mass loading of the catalyst on CC. F (96500 C mol^{-1}) is the Faraday constant, Q (C) is the quantity of applied electricity.

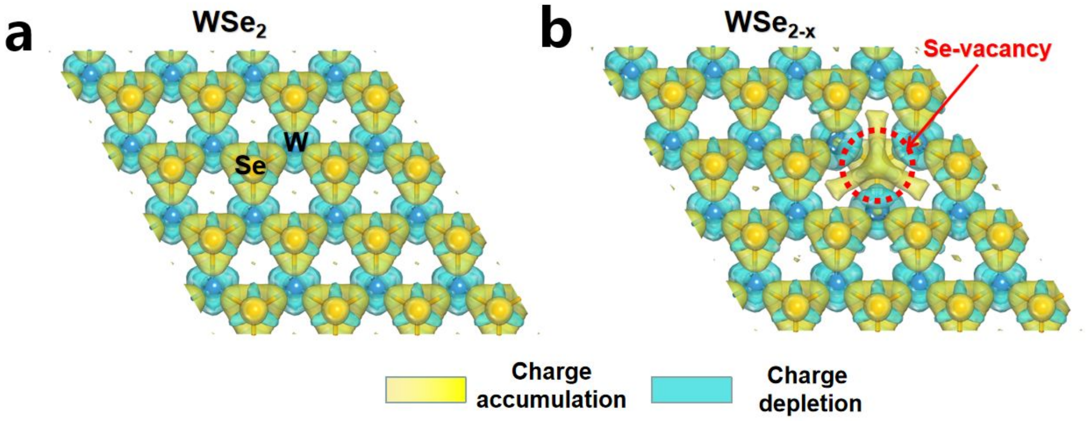

Figure S1. Differential charge density of (a) WSe_2 (001) and (b) WSe_{2-x} (001).

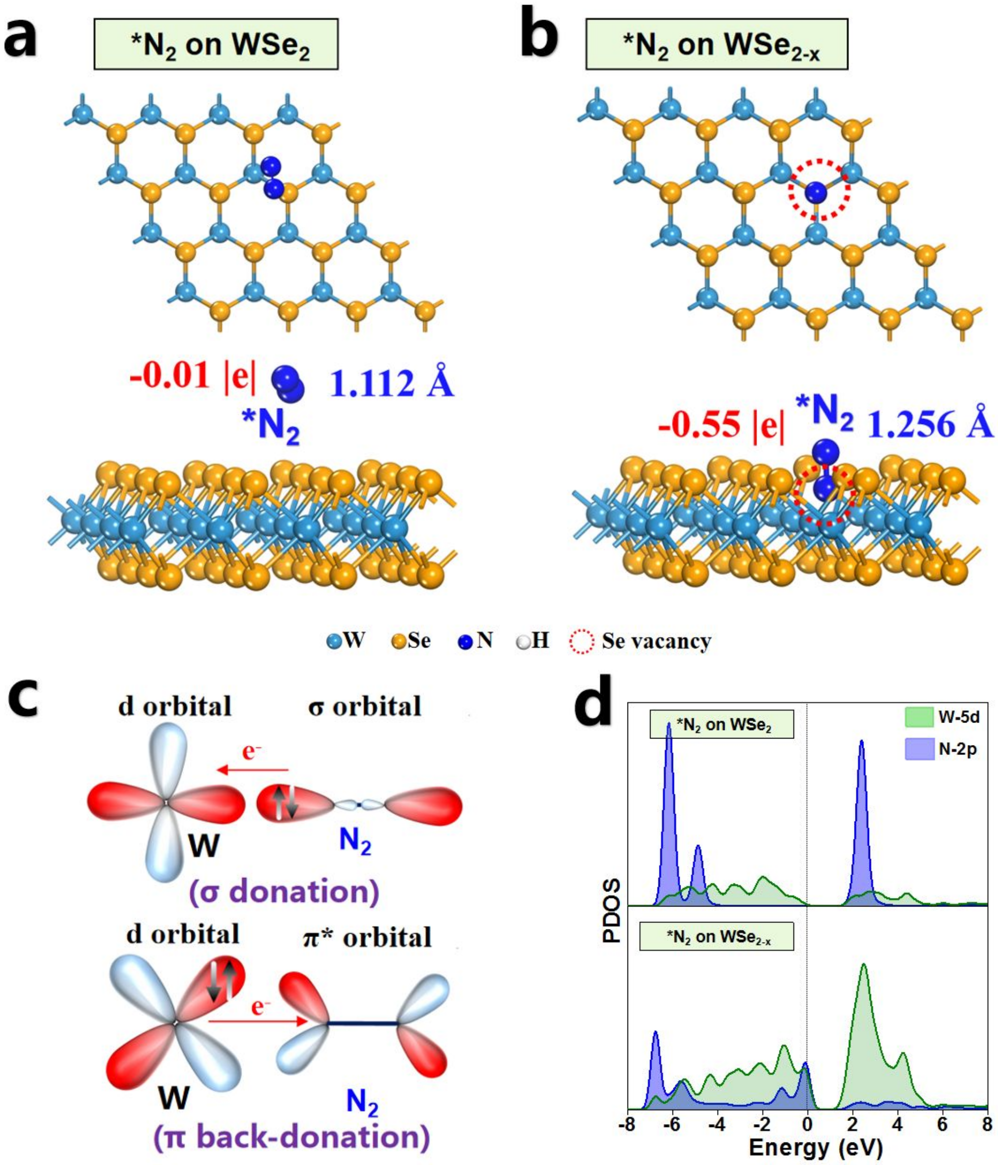

Figure S2 (a, b) Optimized structures of $*N_2$ on WSe_2 and WSe_{2-x}. (c) Schematic of N_2 bonding state with W active sites. (d) PDOS of $*N_2$ on WSe_2 and WSe_{2-x}.

As shown in Figure S2a, the adsorption of N_2 on pristine WSe_2 is restricted by the surface-terminated Se atoms, as indicated by a very small N-N elongation (1.112 Å) and the negligible electron transfer (-0.01 |e|). Noticeably, upon introducing a Se-vacancy in WSe_{2-x} (Figure S2b), N_2 can be preferentially trapped into the S-vacancy site where $*N_2$ is bonded with three unsaturated W atoms (W-W-W trimer) through an "acceptance-donation" mechanism (Figure S2c). In this condition, the S-vacancy-induced W-W-W trimer active sites inject a large net charge of -0.55 |e| into $*N_2$ whose N≡N bond length is remarkably elongated to 1.256 Å. PDOS analysis (Figure S2d) also confirms the greatly promoted N_2 adsorption over W-W-W trimer, showing that W-5d band is well overlapped with N-2p band, whereas a poor W-5d/N-2p band overlapping is displayed for pristine WSe_2.

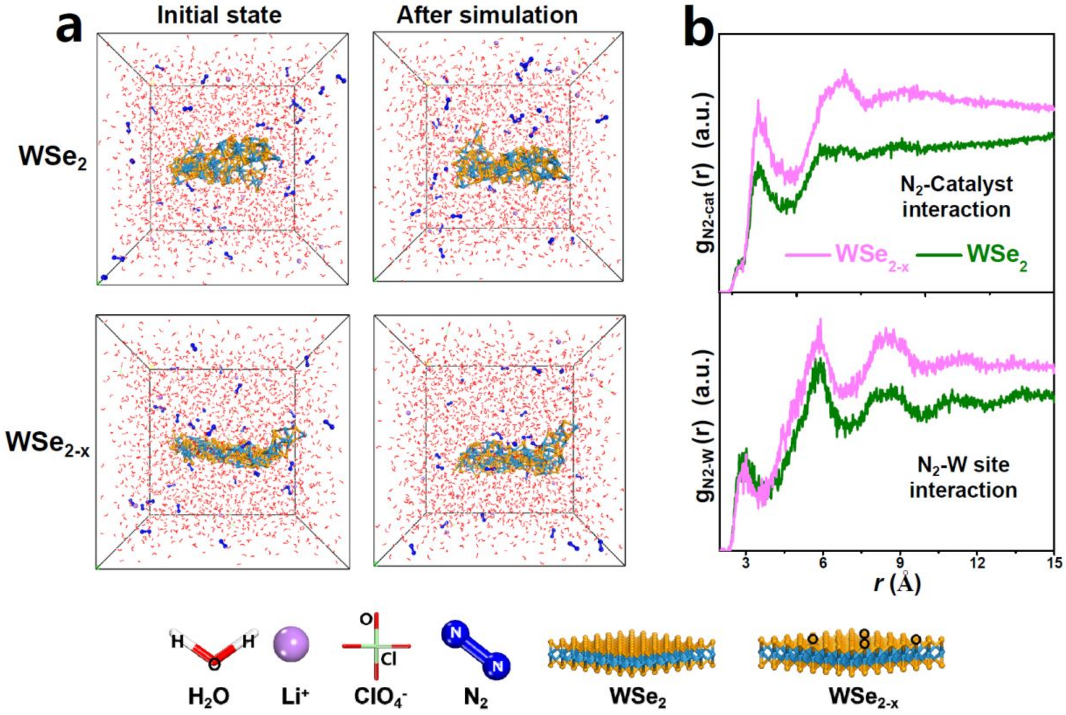

Figure S3. (a) Snapshots for the dynamic process of N_2 adsorption on WSe_2 (top) and WSe_{2-x} (bottom) after 5 ns MD simulations. (b) Comparison for the RDF curves of N_2-catalyst interaction (top) and N_2-W site interaction (bottom) for WSe_2 and WSe_{2-x}.

The above MD simulations show that compared to WSe_2, WSe_{2-x} ensures enhanced N_2-catalyst and N_2-W site interactions, indicating that WSe_{2-x} facilitates the N_2 adsorption.

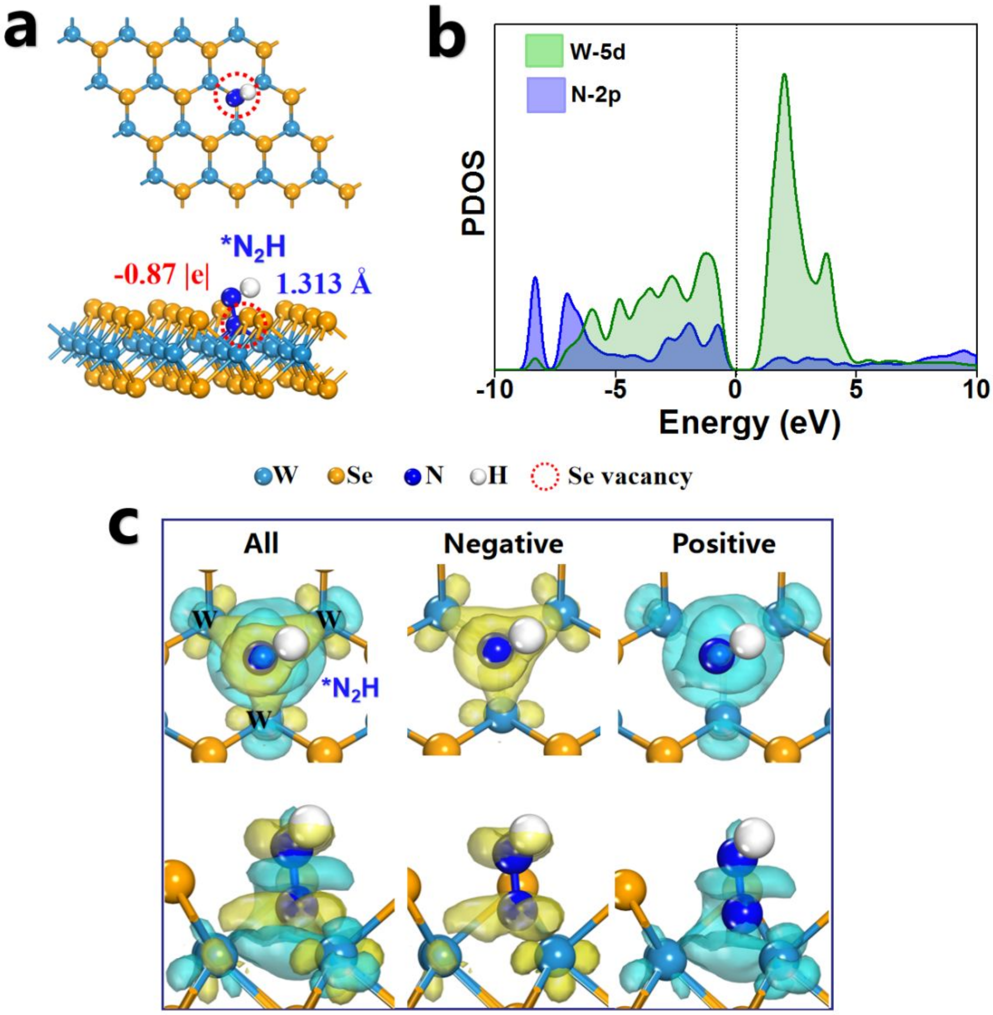

Figure S4. (a) Optimized structures of $*N_2H$ on WSe_2 and WSe_{2-x}. (b) PDOS of $*N_2H$ on WSe_{2-x}. (c) Differential charge density of $*N_2H$ on WSe_{2-x}. Yellow: electron accumulation, cyan: electron depletion.

As shown in Figure S4a, the Se-vacancy induced W-W-W trimer can well stabilize the $*N_2H$ by donating a considerable net charge of -0.87 |e| into $*N_2H$ with the N≡N bond length further largely stretched to 1.313 Å. This results in a remarkable W-5d/N-2p orbital overlapping between $*N_2H$ and W-W-W trimer (Figure S4b). Differential charge density (Figure S4c) further reveals that the $*N_2H$ stabilization enabled by the W-W-W trimer also follows the "acceptance-donation" mechanism where charge accumulation/depletion takes place around both $*N_2H$ and W-W-W trimer. The above findings demonstrate that the Se-vacancy-induced W-W-W trimer can serve as ternary-active-centers to strongly activate the N_2 and promote the $*N_2H$ formation, in favor of the largely enhanced NRR activity of WSe_{2-x}.

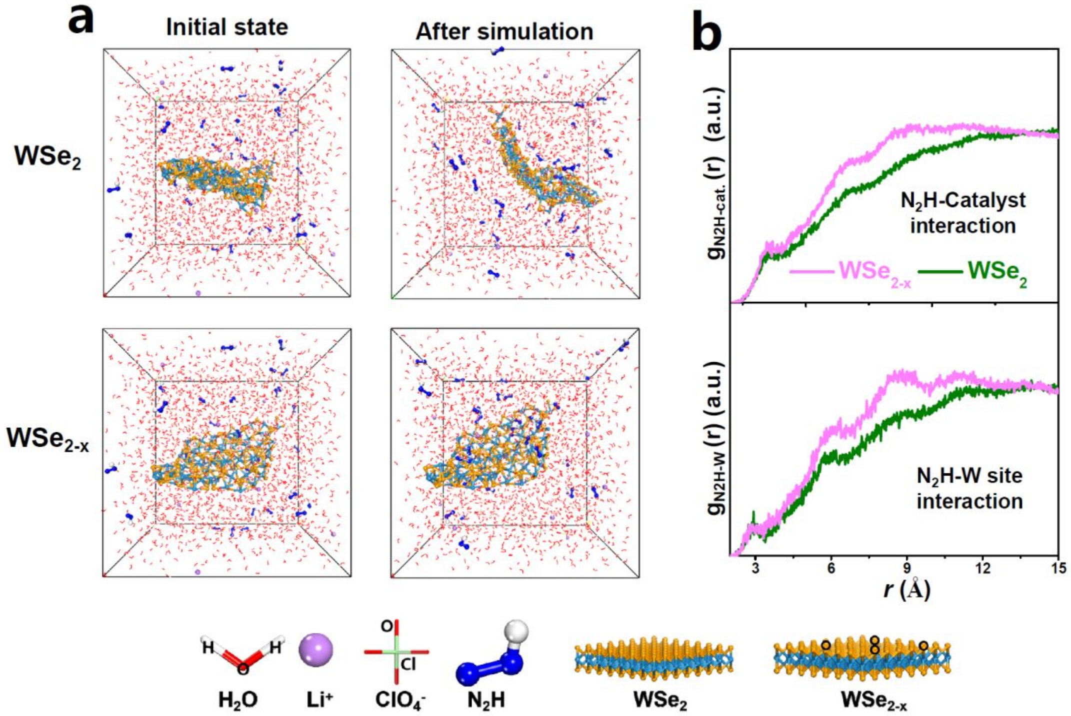

Figure S5. (a) Snapshots for the dynamic process of N_2H adsorption on WSe_2 (top) and WSe_{2-x} (bottom) after 5 ns MD simulations. (b) Comparison for the RDF curves of N_2H-catalyst interaction (top) and N_2H-W site interaction (bottom) for WSe_2 and WSe_{2-x}.

The above MD simulations shows that compared to WSe_2, WSe_{2-x} renders enhanced N_2H-catalyst and N_2H-W site interactions, suggesting that WSe_{2-x} facilitates the $*N_2H$ formation.

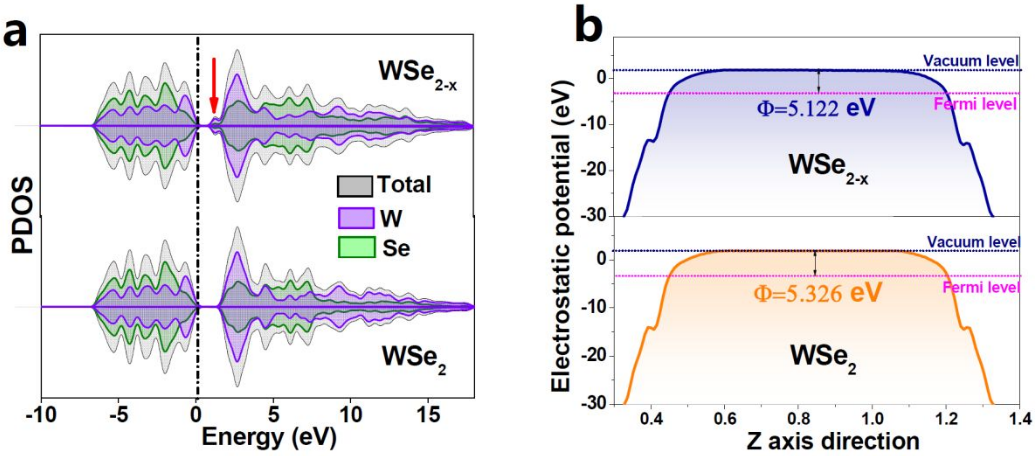

Figure S6. (a) PDOS of WSe$_2$ and WSe$_{2-x}$. (b) Average potential profiles of WSe$_2$ and WSe$_{2-x}$.

PDOS analysis (Figure S6a) shows that in comparison with the semiconducting WSe$_2$ with a noticeable band gap, a new defect level (marked by a red arrow) appears at the conduction band minimum of WSe$_{2-x}$. This Se-vacancy-induced defect level can not only reduce the band gap to boost the charge transfer efficiency, but also facilitate the NRR process by offering more charge carriers for the activation of N$_2$[6]. Moreover, the calculated average potential profiles (Figure S6b) show that WSe$_{2-x}$ exhibits a lower work function (5.122 eV) than WSe$_2$ (5.326 eV), which demonstrates the stronger ability of WSe$_{2-x}$ for promoting the electron transfer from catalyst surface to the absorbed N$_2$ and intermediates[7].

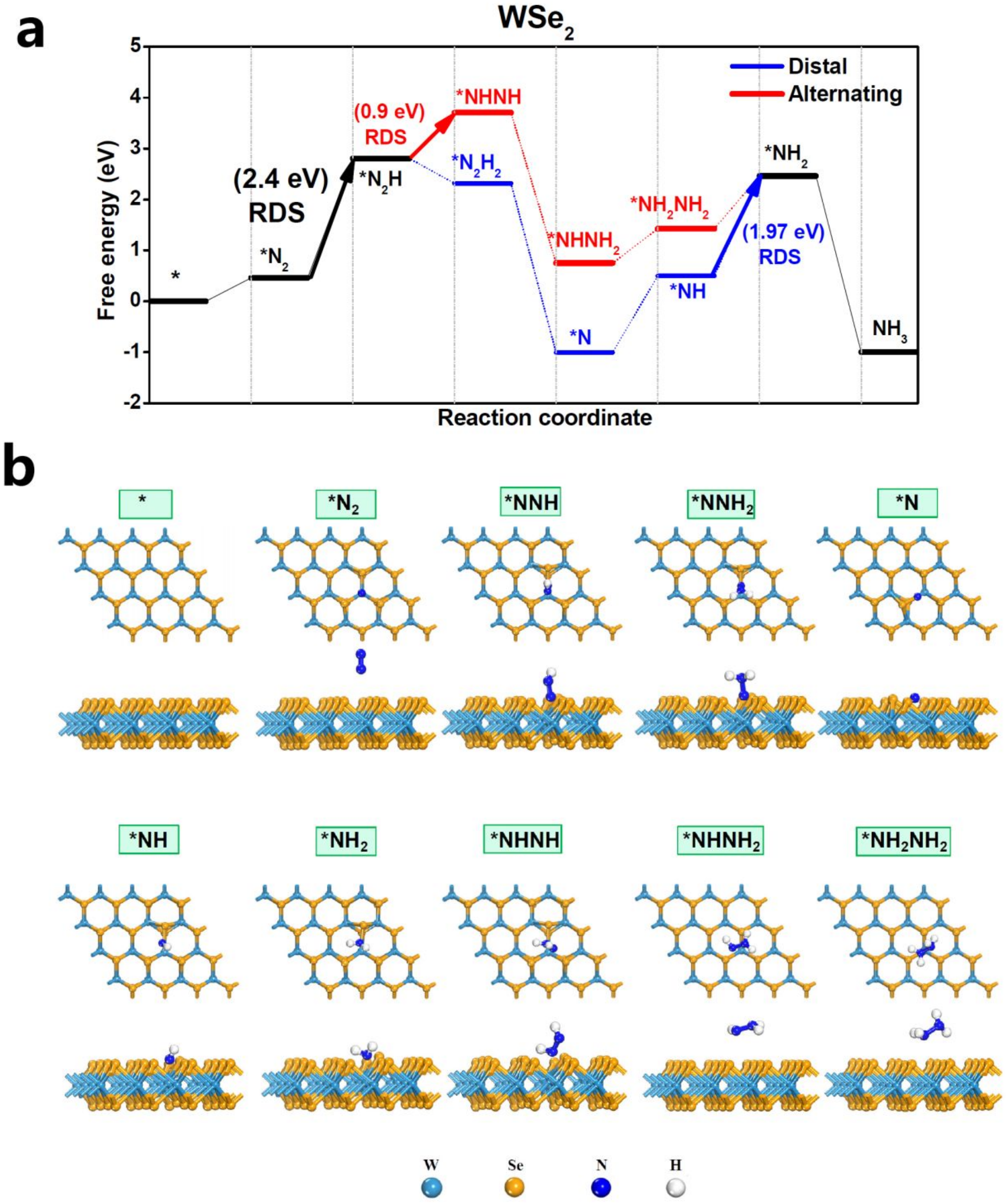

Figure S7. (a) Free energy diagrams of distal and alternating NRR pathways on WSe$_2$ at $U = 0$, and (b) corresponding optimized structures of NRR intermediates.

The free energy diagrams demonstrate that the alternating pathway is energetically preferred for WSe$_2$ with a lower energy barrier (0.9 eV), but the overall energy barrier is the same (*N$_2$→*N$_2$H, 2.4 eV) for both distal and alternating NRR pathways.

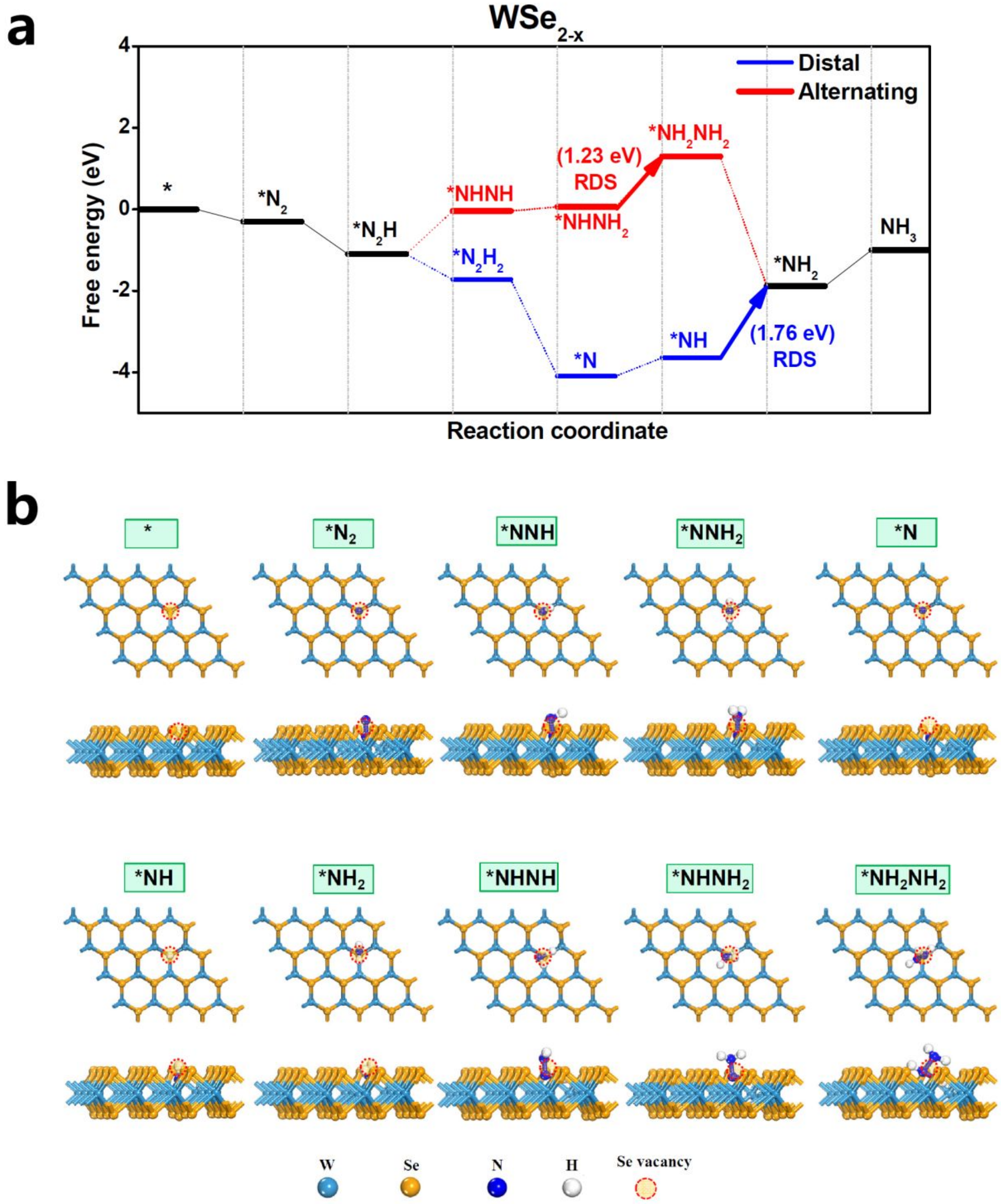

Figure S8. (a) Free energy diagrams of distal and alternating NRR pathways on WSe_{2-x} at $U = 0$, and (b) corresponding optimized structures of NRR intermediates.

The free energy diagrams demonstrate that the alternating pathway is energetically preferred for WSe_{2-x} with a lower energy barrier ($^*NHNH_2 \rightarrow {}^*NH_2NH_2$, 1.23 eV) which is also the overall energy barrier.

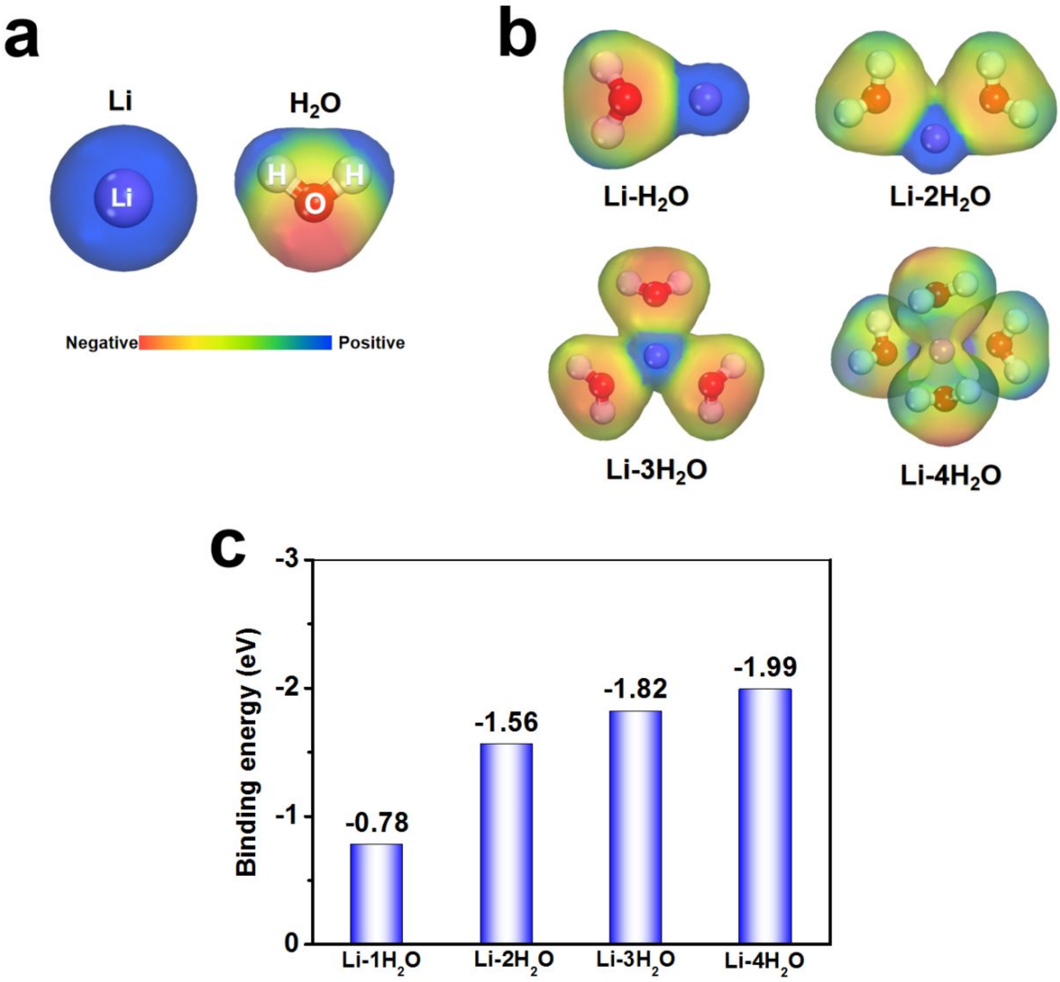

Figure S9. (a) ESP of Li atom and H_2O molecule. (b) ESP of Li-H_2O interactions with different numbers of H_2O molecules (1-4), and (c) corresponding binding energies.

The ESP diagrams show that Li cation is preferentially coordinated with four neighboring H_2O molecules (Li-4H_2O) due to the largest electron cloud overlapping (Figure S9b) and the highest binding energy between Li and H_2O molecules (Figure S9c).

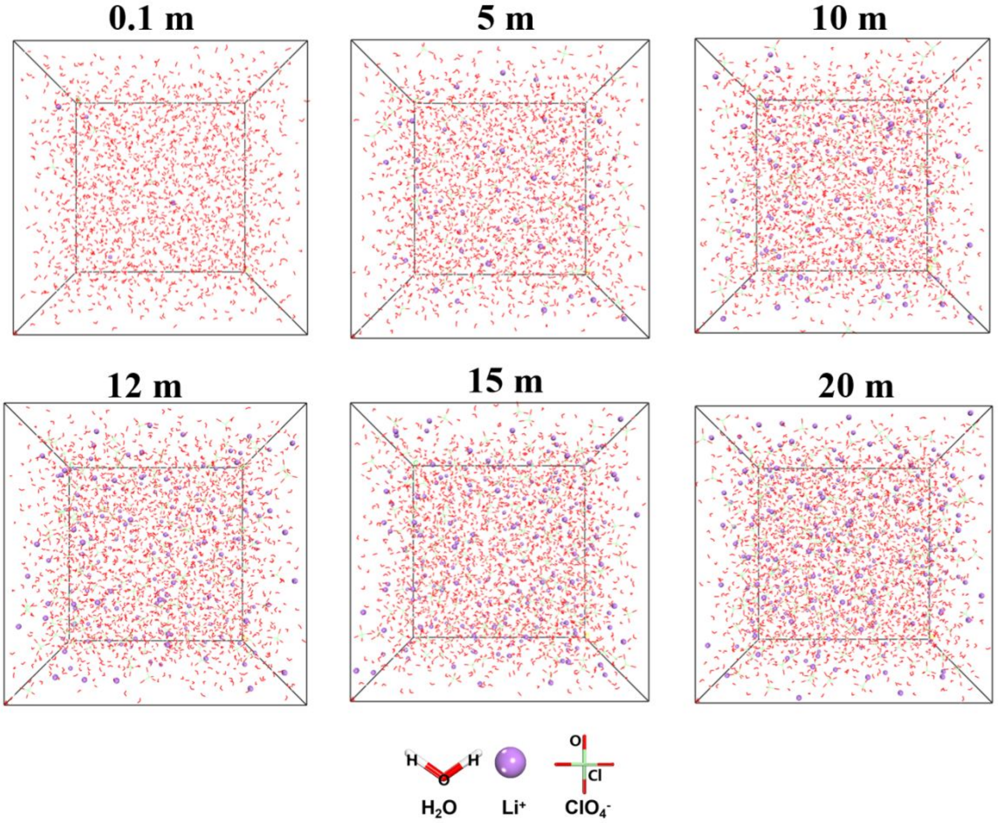

Figure S10. Snapshots for the 0.1-20 m $LiClO_4$ electrolytes after 5 ns MD simulations.

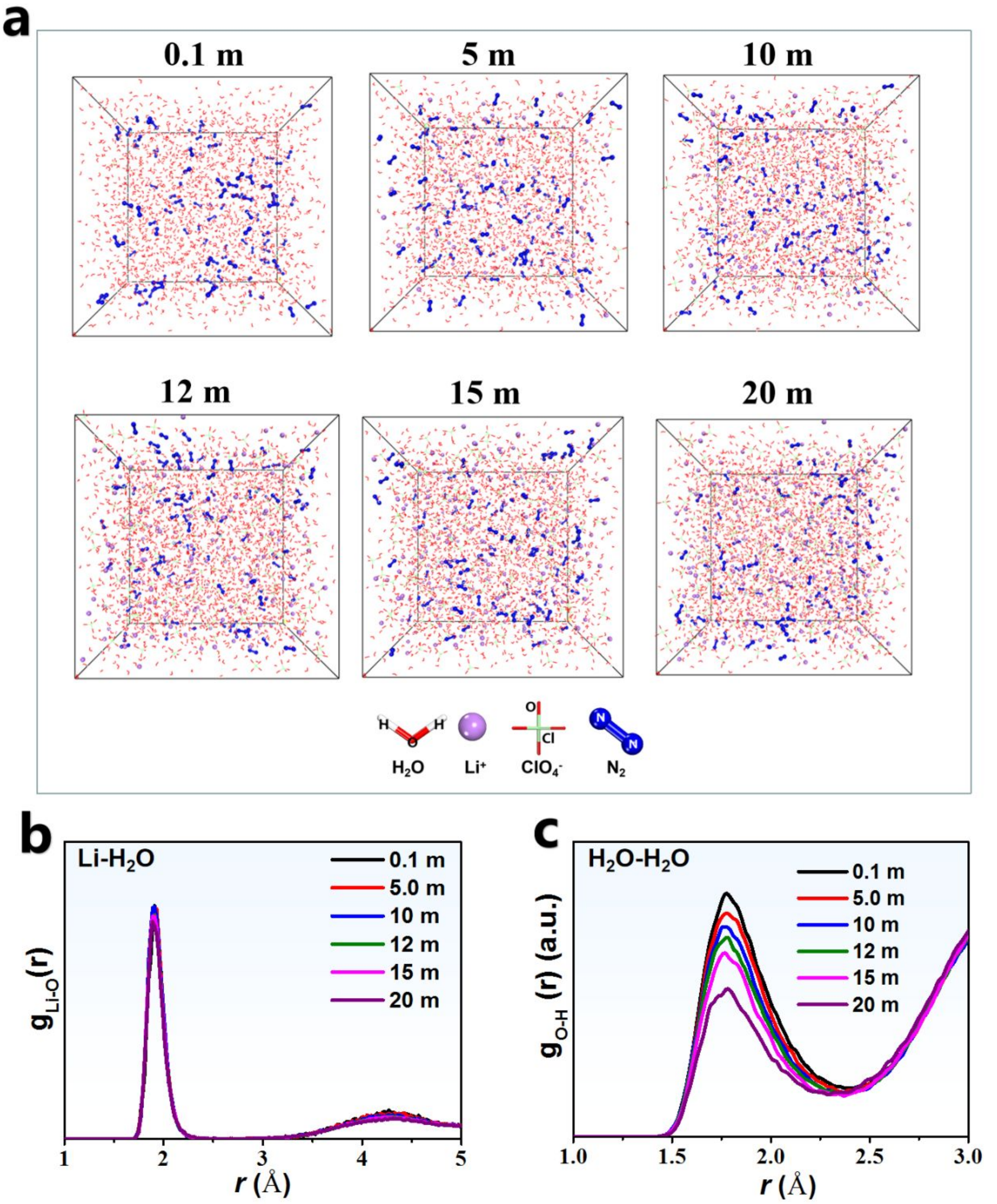

Figure S11. (a) Snapshots for the 0.1-20 m $LiClO_4$ electrolytes (each containing 100 N_2 molecules) after 5 ns MD simulations, and corresponding RDF curves of (b) Li-H_2O and (c) H_2O-H_2O interactions.

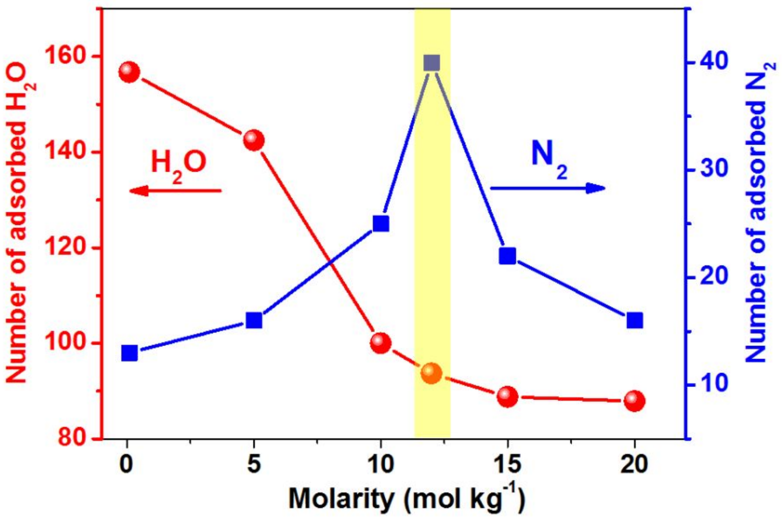

Figure S12. Estimated number of N_2 and free H_2O molecules absorbed on the catalyst at different concentrations of electrolytes based on the corresponding snapshots (Figure 2f).

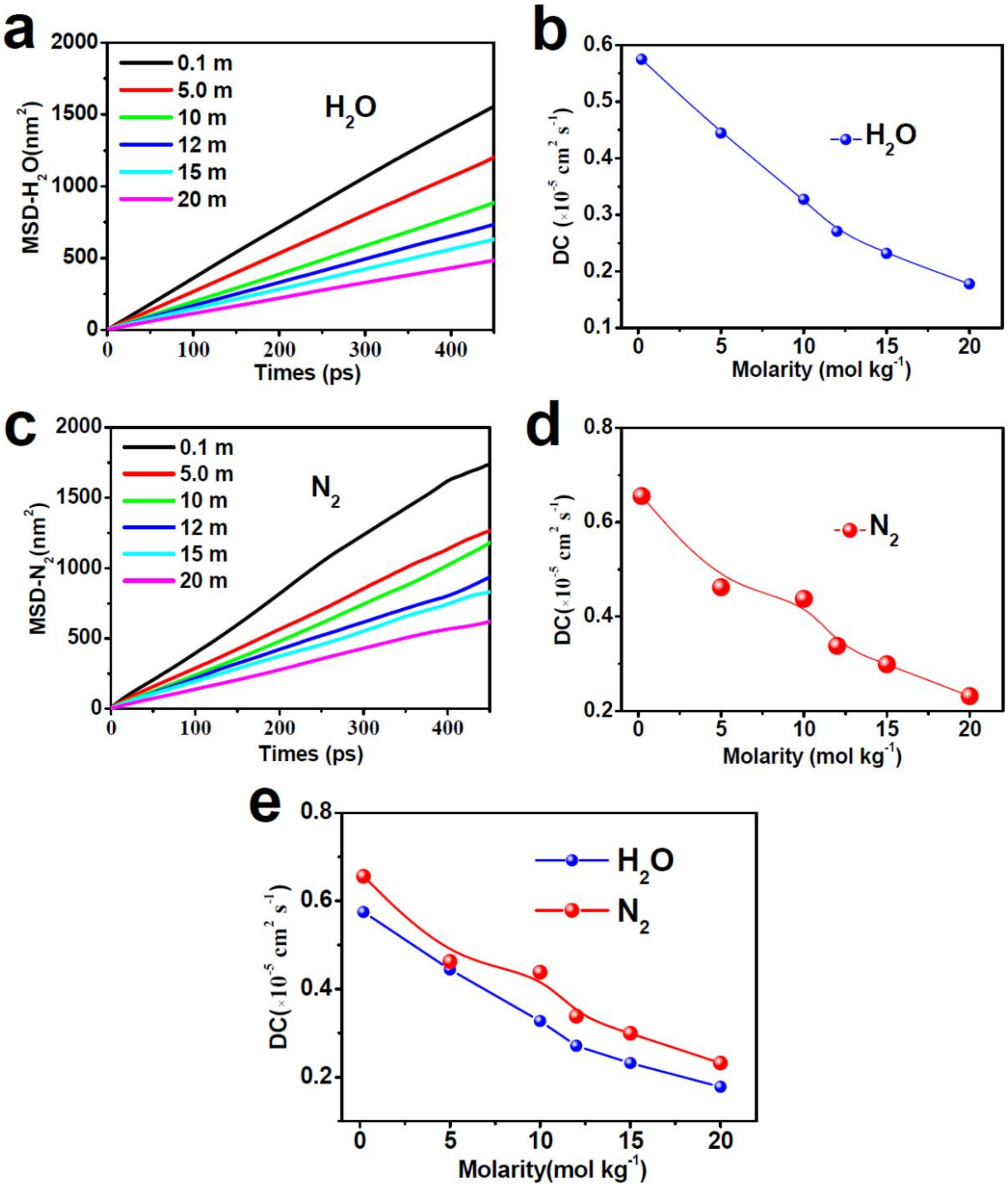

Figure S13. (a, c) Mean square displacements (MSD) and corresponding (b, d, e) diffusion coefficients (DCs) of H_2O and N_2 in 0.1-20 m $LiClO_4$ electrolytes.

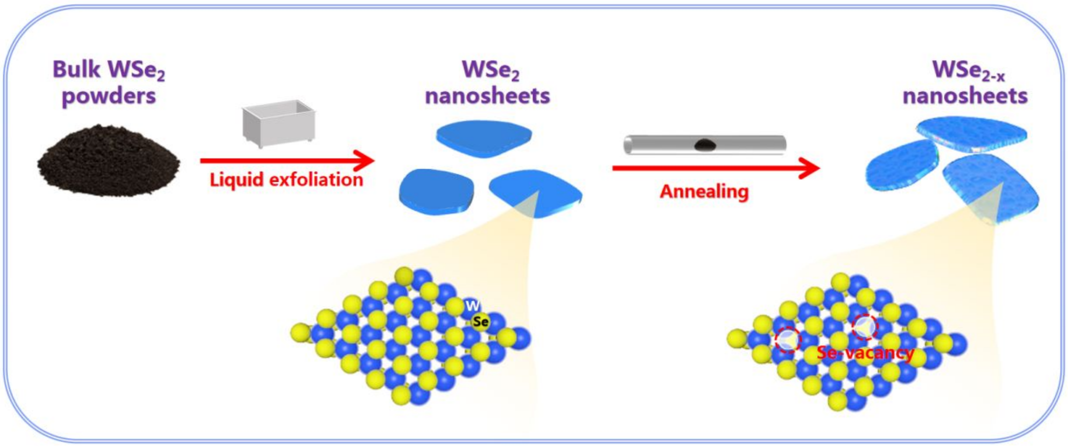

Figure S14. Schematic of the synthesis process of WSe_{2-x}.

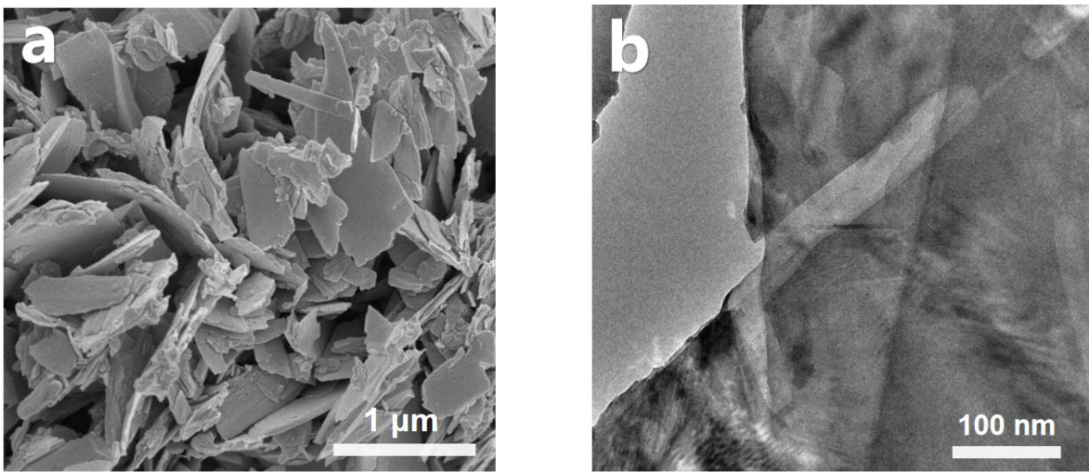

Figure S15. (a) SEM and (b) TEM images of WSe_2 nanosheets.

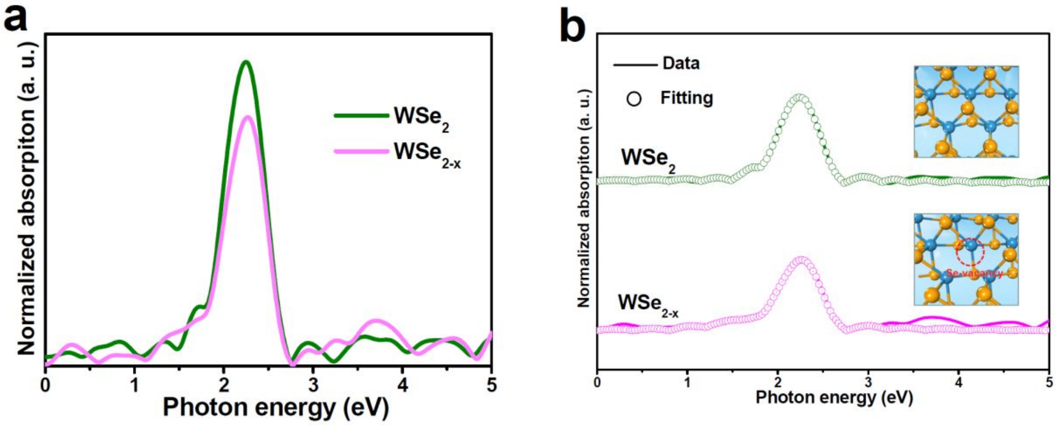

Figure S16. (a) W L3-edge EXAFS spectra of WSe$_2$ and WSe$_{2-x}$, and (b) EXAFS fitting curves using the corresponding structural models (inset).

Table S1. Structural parameters extracted from the W L3-edge EXAFS fitting.

Sample	Path	CN	R (Å)	σ^2 (10^{-3}Å)	ΔE_0 (eV)	R factor
WSe$_2$	W-Se	5.96	2.53	5.1	-3.3	0.005
WSe$_{2-x}$	W-Se	5.38	2.55	6.2	-3.8	0.008

CN is the coordination number; R is interatomic distance; σ^2 is Debye-Waller factor; ΔE_0 is edge-energy shift; R factor is used to value the goodness of the fitting. The amplitude reduction factor is 0.89.

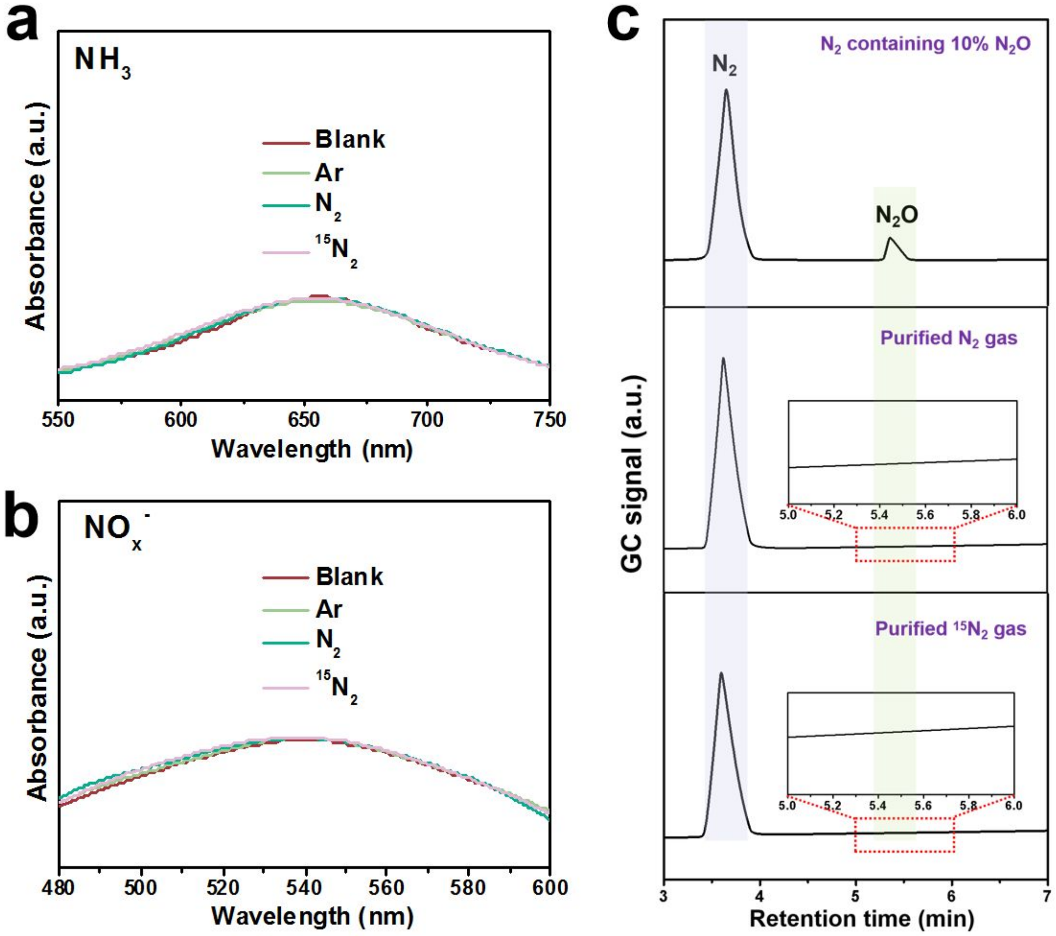

Figure S17. UV-vis absorption spectra for the determination of (a) NH_3 and (b) NO_x^- contaminants in deionized water solution (blank) and tested electrolytes after passing various feeding gas (Ar, N_2 and $^{15}N_2$) through the acid (0.05 M H_2SO_4) and alkaline (0.1 M KOH) traps. (c) Gas chromatography spectra of 10% N_2O in N_2, purified N_2 and purified $^{15}N_2$.

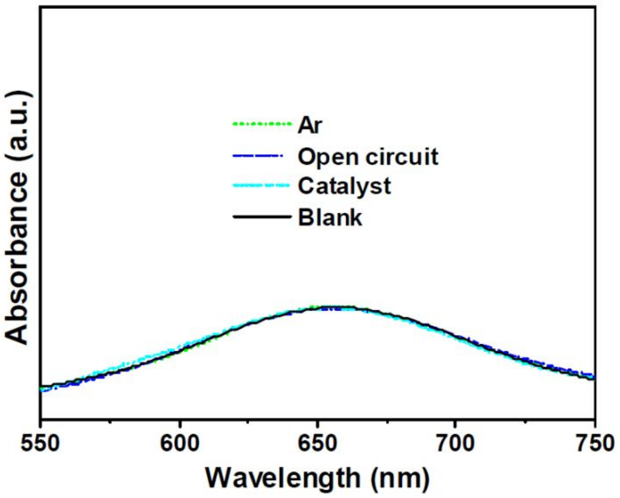

Figure S18. UV-vis absorption spectra of working electrolytes after 2 h of electrolysis in Ar-saturated solutions on WSe_{2-x} at -0.5 V, N_2-saturated solution on WSe_{2-x} at open circuit, and reference UV-vis absorption spectra of deionized water solution (blank), and catalyst testing (immersing working electrode (coating catalyst) in deionized water solution for 6 h and then testing the UV-vis absorption spectra of resulting electrolyte).

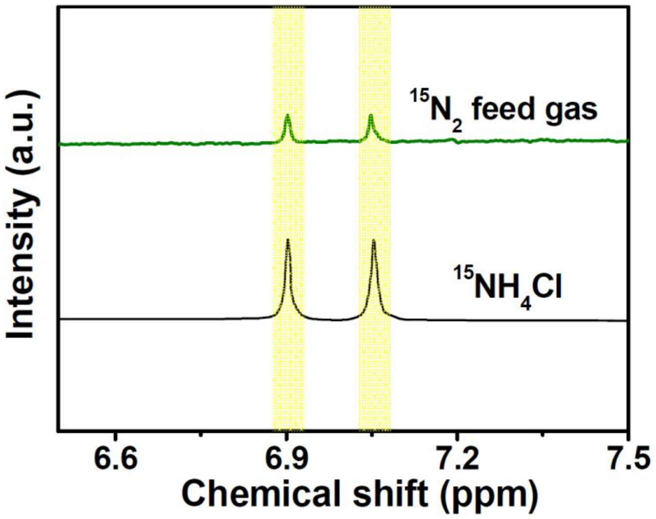

Figure S19. Isotope-labeling NMR spectra of the electrolytes fed by $^{15}N_2$ and standard sample.

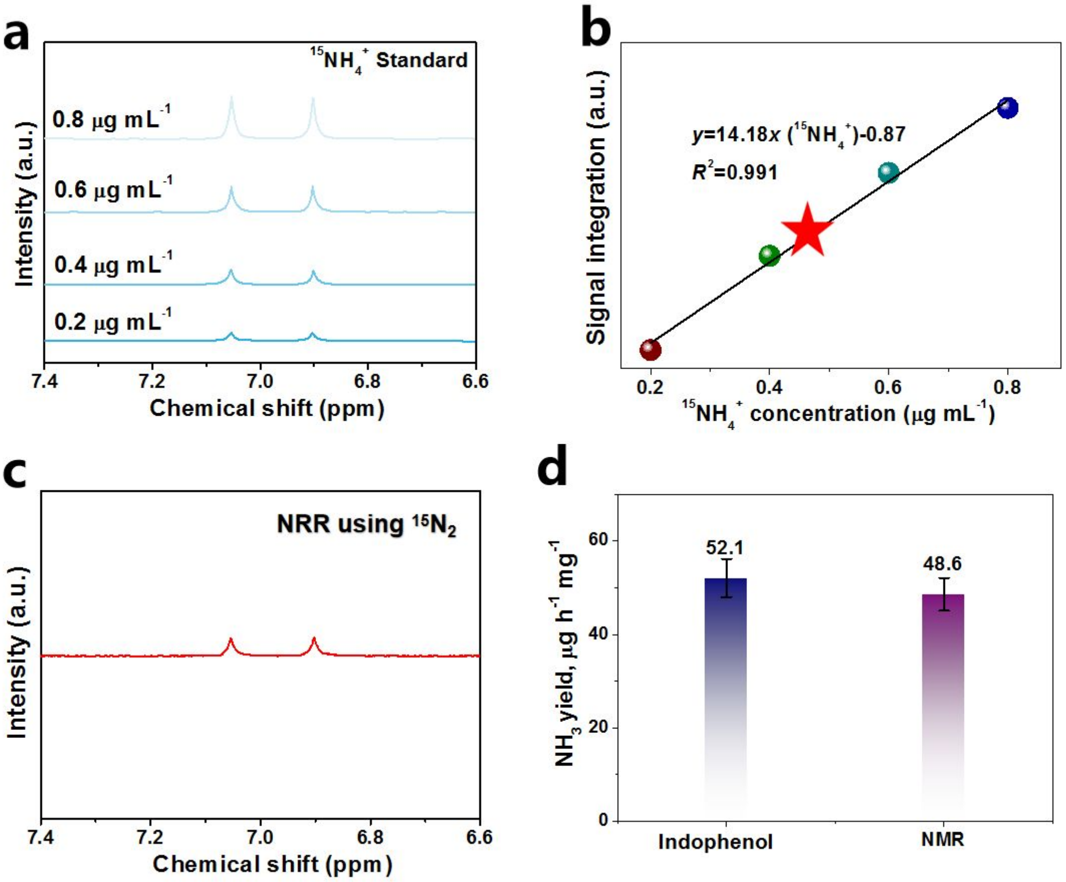

Figure S20. (a) ^{1}H NMR spectra of $^{15}NH_4^+$ standard samples with different concentrations, and (b) corresponding calibration curve of $^{15}NH_4^+$ concentration vs. peak area, red star represents the $^{15}NH_4^+$ concentration derived from the NRR fed by $^{15}N_2$ over WSe_{2-x} at -0.5 V for 2 h (c). (d) Comparison of the $^{15}NH_3$ yield of WSe_{2-x} obtained from the indophenol and NMR methods (in 0.5 m $LiClO_4$).

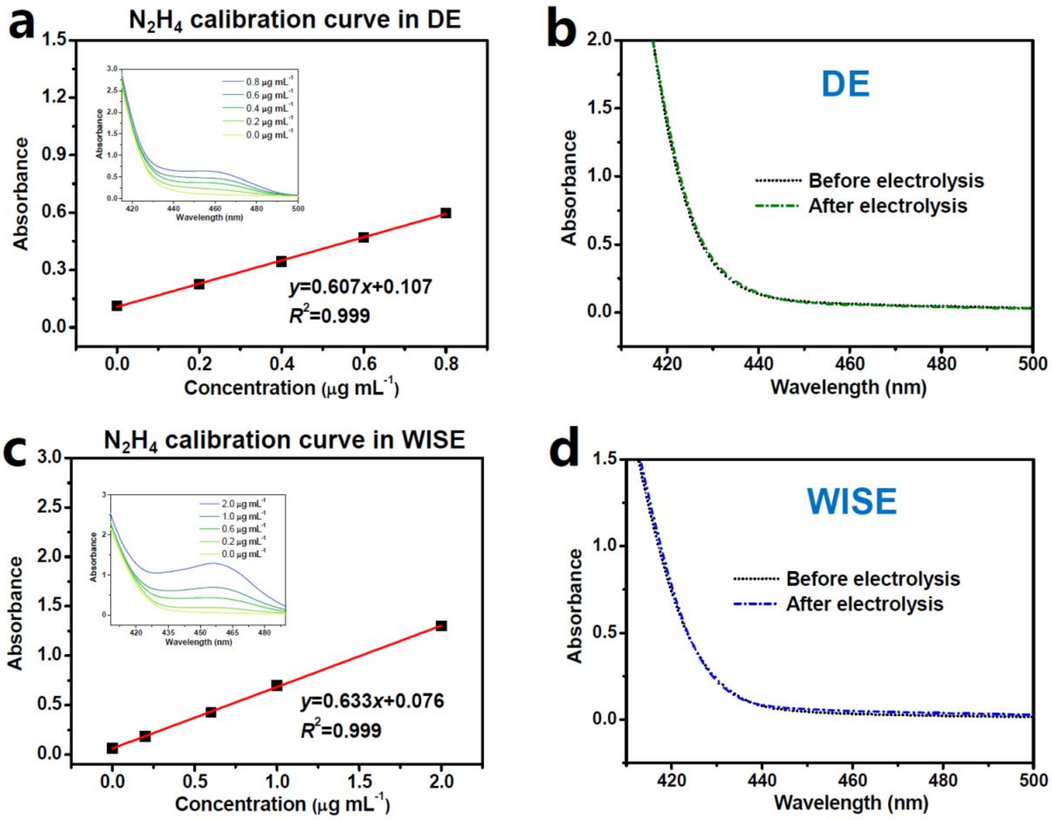

Figure S21. (a, c) N_2H_4 calibration curves in DE and WISE, and (b, d) corresponding UV-vis spectra of the electrolytes (stained with the chemical indicator based on the method of Watt and Chrisp) before and after 2 h of NRR electrolysis on WSe_{2-x} in DE and WISE at -0.5 V.

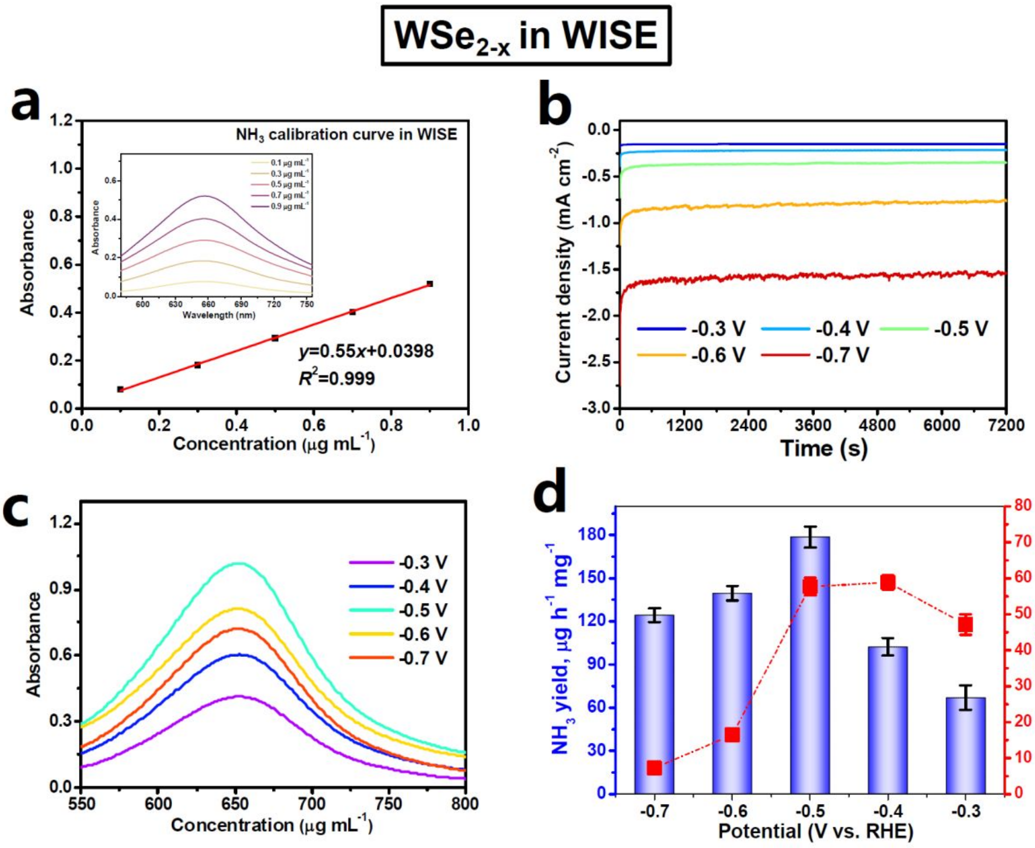

Figure S22. (a) NH_3 calibration curve in WISE. (b) Chronoamperometry curves at various potentials after 2 h of NRR electrolysis over WSe_{2-x} in WISE, and corresponding (c) UV-vis absorption spectra, and (d) obtained NH_3 yields and FEs.

WSe_{2-x} in DE

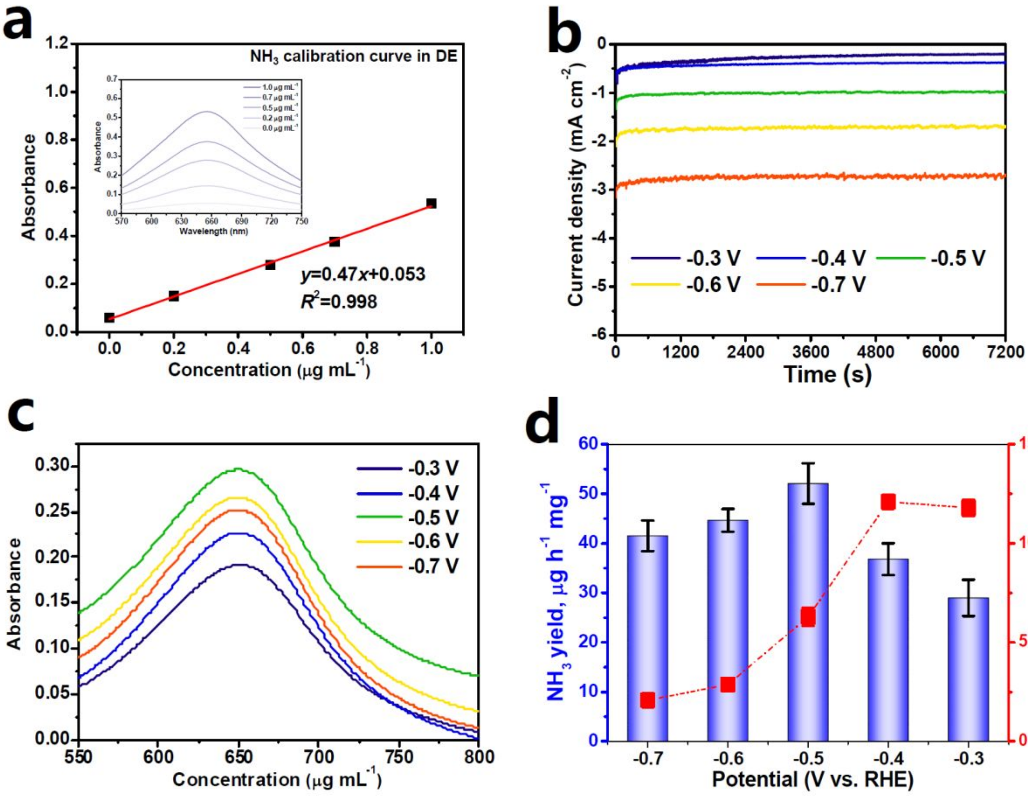

Figure S23. (a) NH_3 calibration curve in DE. (b) Chronoamperometry curves at various potentials after 2 h of NRR electrolysis over WSe_{2-x} in DE, and corresponding (c) UV-vis absorption spectra, and (d) obtained NH_3 yields and FEs.

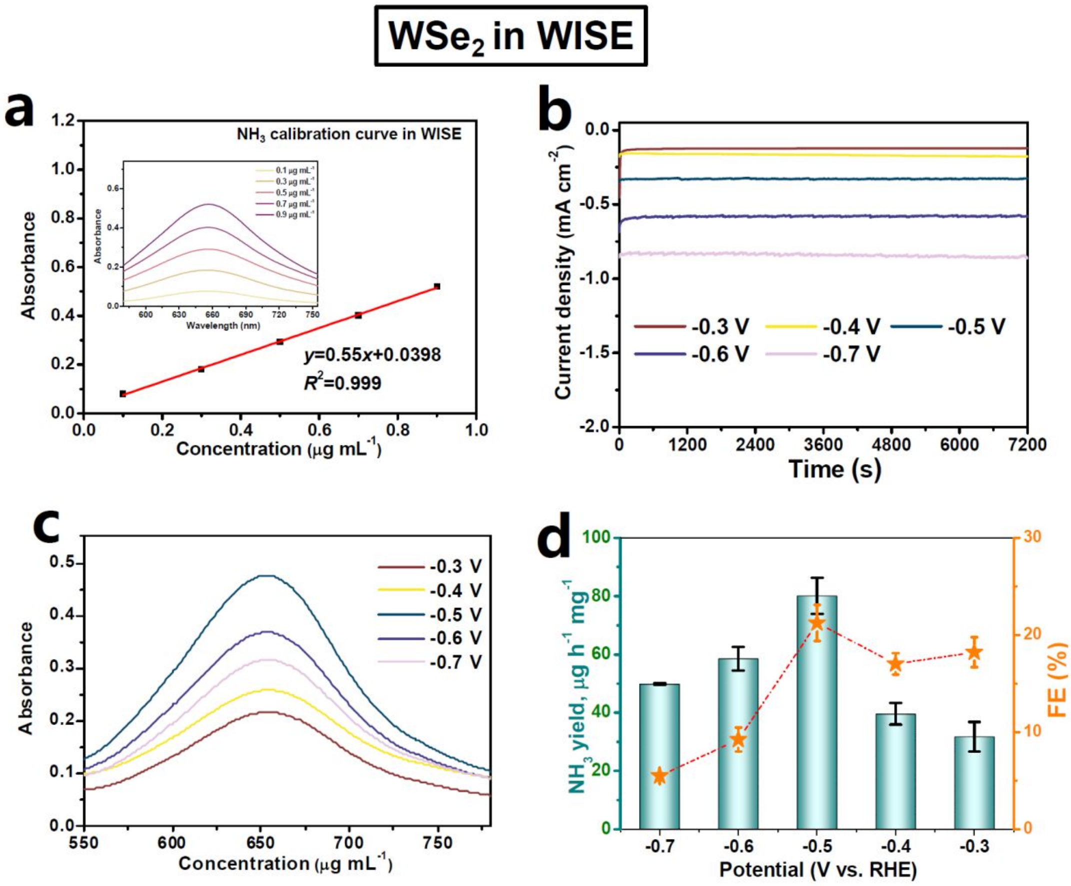

Figure S24. (a) NH_3 calibration curve in WISE. (b) Chronoamperometry curves at various potentials after 2 h of NRR electrolysis over WSe_2 in WISE, and corresponding (c) UV-vis absorption spectra, and (d) obtained NH_3 yields and FEs.

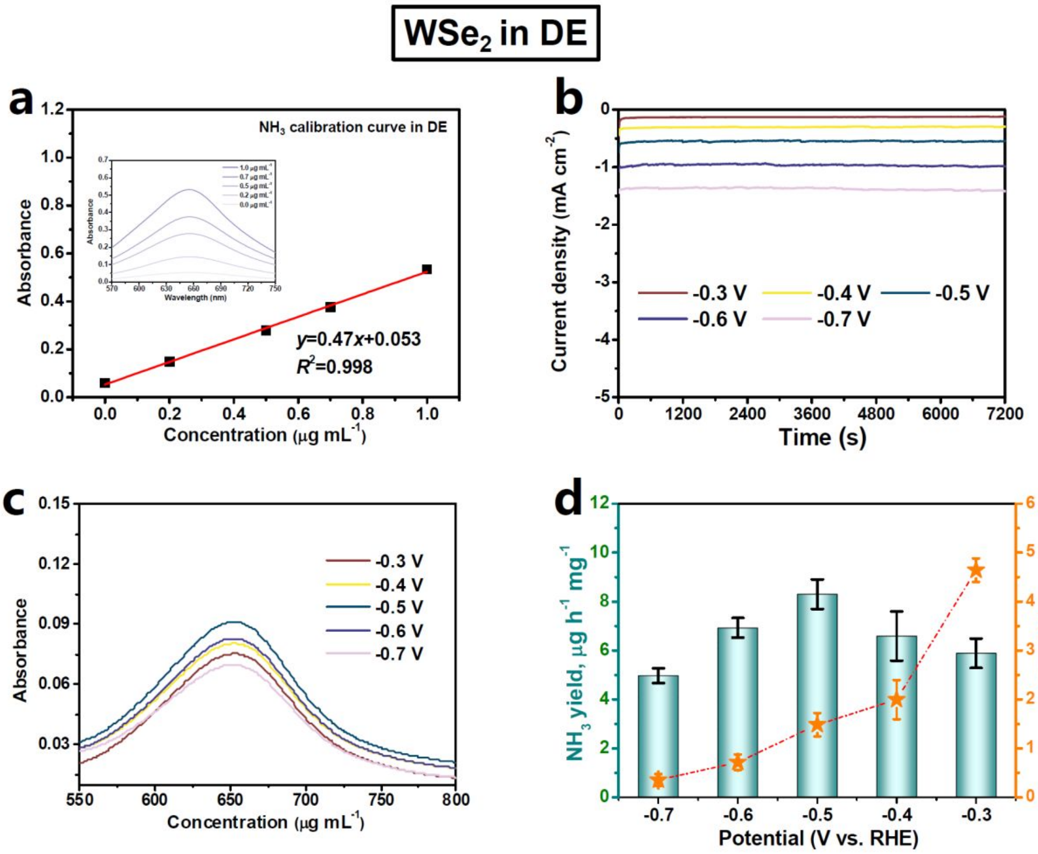

Figure S25. (a) NH_3 calibration curve in DE. (b) Chronoamperometry curves at various potentials after 2 h of NRR electrolysis over WSe_2 in DE, and corresponding (c) UV-vis absorption spectra, and (d) obtained NH_3 yields and FEs.

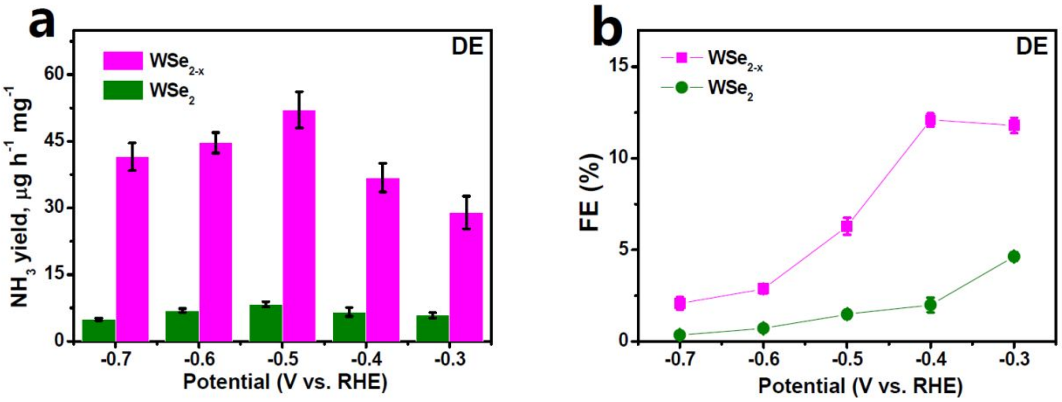

Figure S26. (a) NH_3 yields and (b) FEs of WSe_2 and WSe_{2-x} in DE at various potentials.

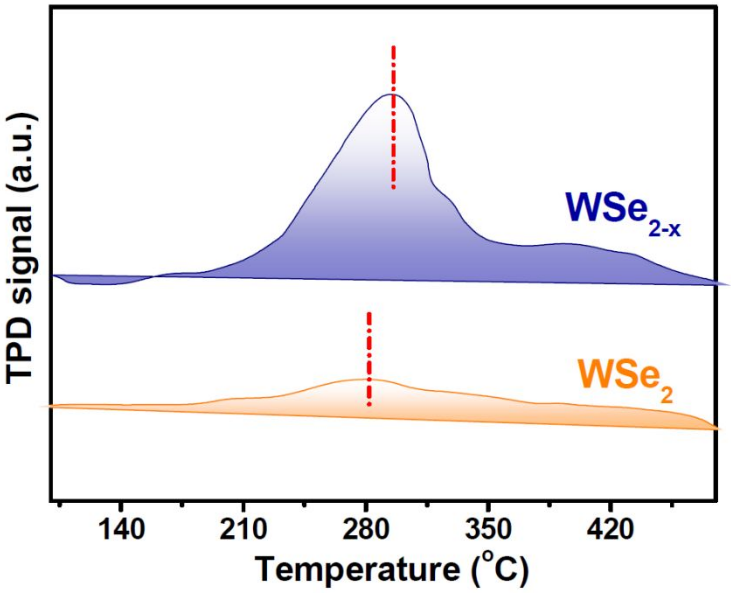

Figure S27. N_2-TPD spectra of WSe_2 and WSe_{2-x}.

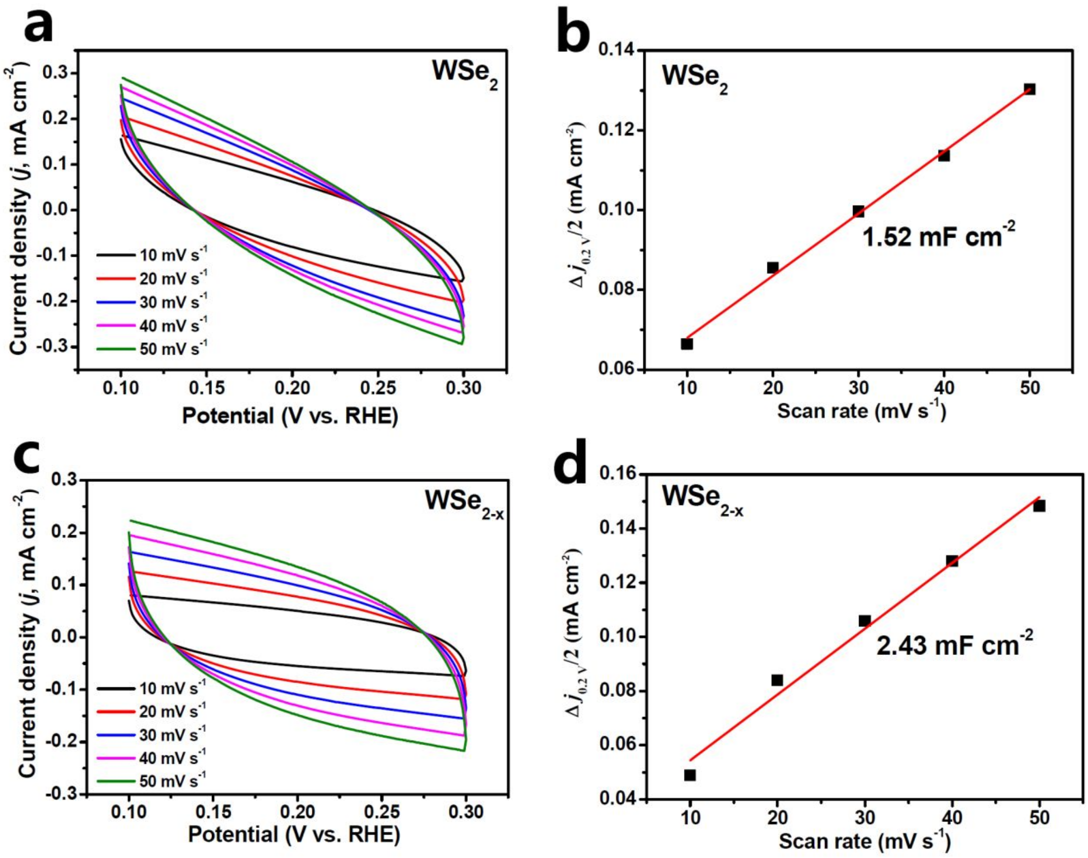

Figure S28. Electrochemical double-layer capacitance (C_{dl}) measurements at different scanning rates of 10~50 mV s^{-1} for (a, b) WSe$_2$ and (c, d) WSe$_{2-x}$.

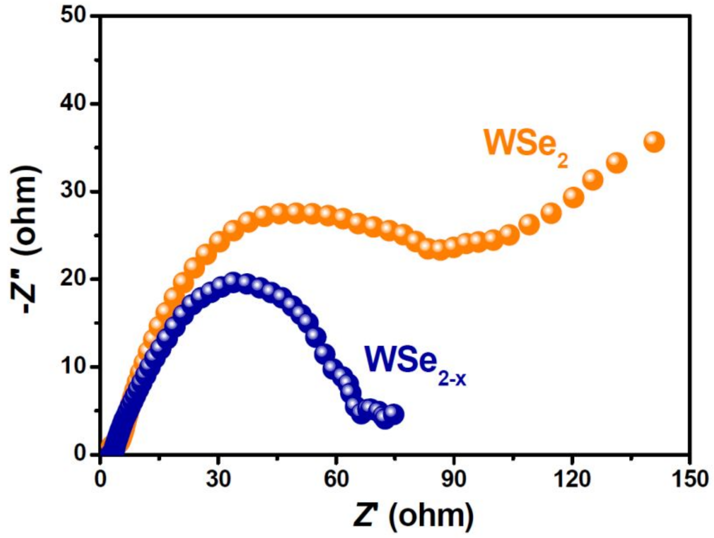

Figure S29. Electrochemical impedance spectroscopy spectra of WSe_2 and WSe_{2-x}.

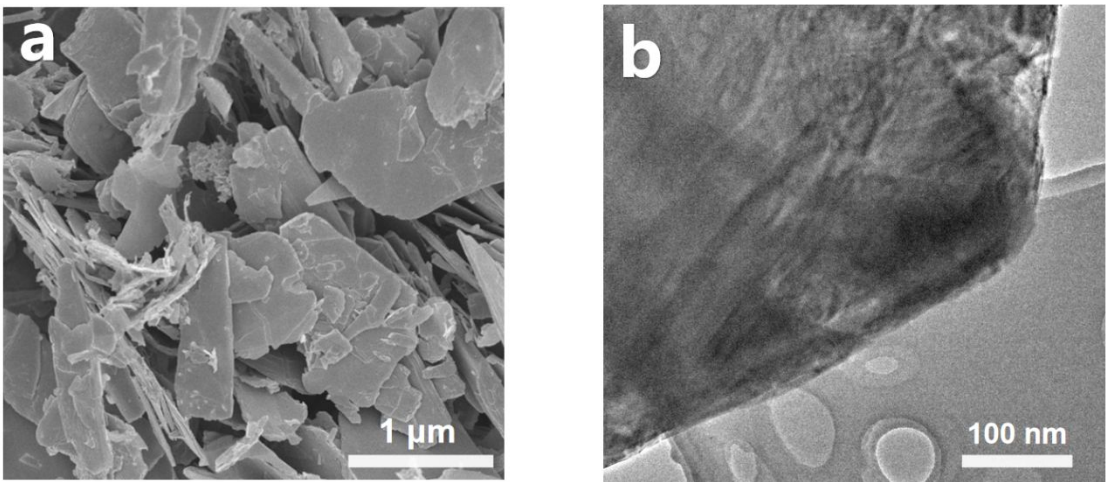

Figure S30. (a) SEM and (b) TEM images of WSe_{2-x} after stability test.

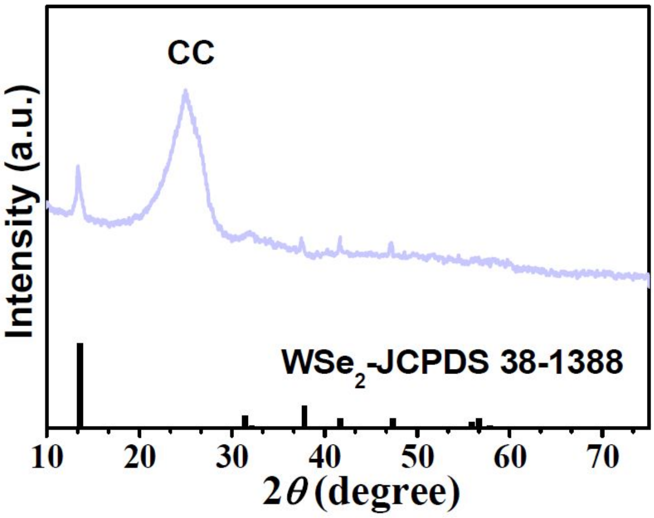

Figure S31. XRD pattern of WSe_{2-x} after stability test.

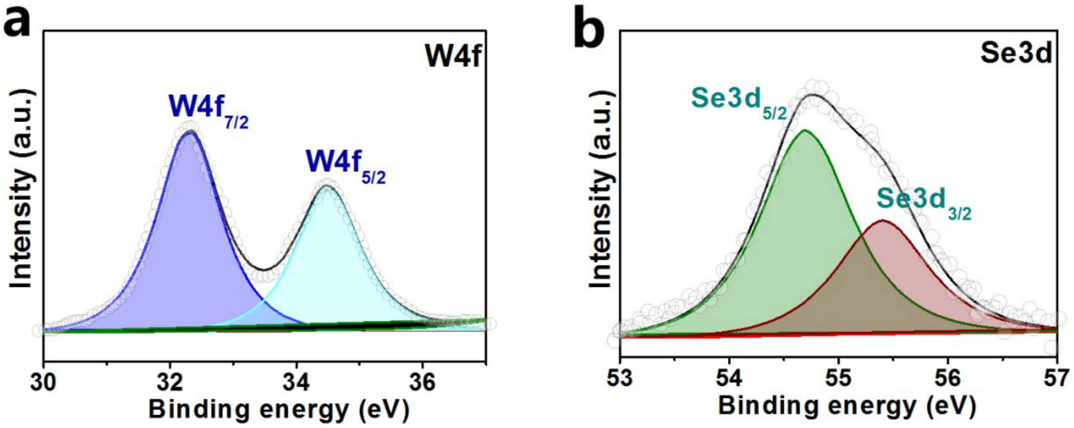

Figure S32. XPS spectra of WSe_{2-x} after stability test: (a) W4f and (b) Se3d.

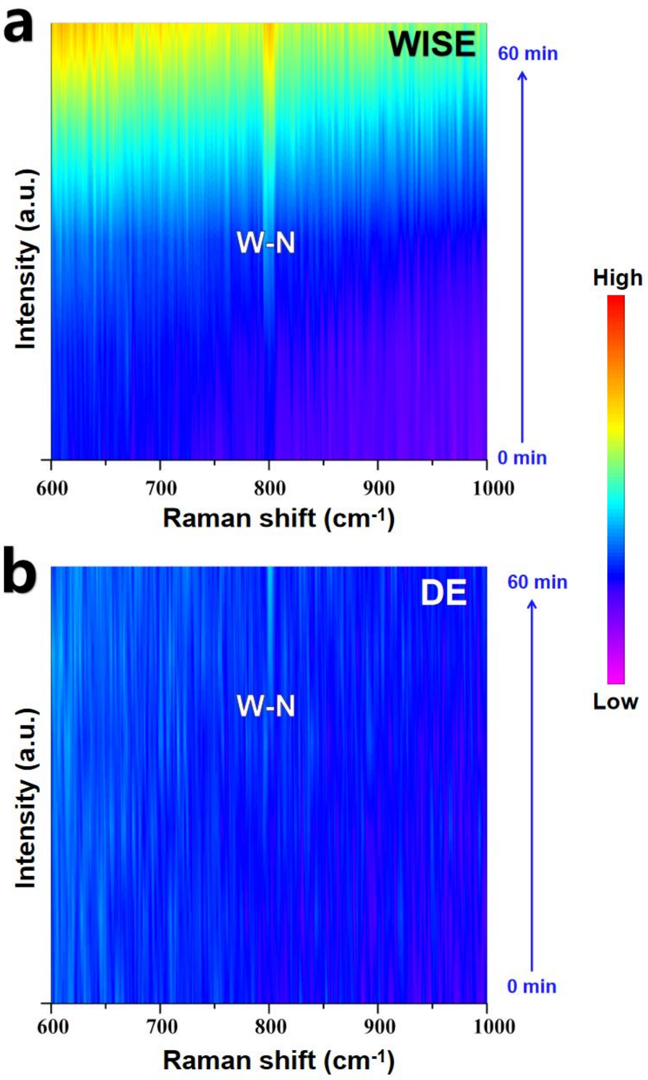

Figure S33. Contour maps of in situ Raman spectra collected during the NRR electrolysis on WSe_{2-x} at 0-60 min in (a) WISE and (b) DE.

Table S2. Comparison of the optimum NH_3 yield and Faradic efficiency (FE) for the high-performing NRR electrocatalysts in general and specific electrolytes at ambient conditions

	Catalyst	**Electrolyte**	**Potential (V vs RHE)**	**NH_3 yield rate (μg h^{-1} mg^{-1})**	**FE(%)**	**Ref.**
General electrolytes	B_4C	0.1 M HCl	-0.75	26.57	15.95	[8]
	Rh-S	0.1 M HCl	-0.25	175.6	13.3	[9]
	Single-atom Ru/Co_3O_4 (Ru_{SAC}/Co_3O_4)	0.1 M KOH	0	39.4	40.2	[10]
	$FeMo_{SAC}/C$	0.25 M $LiClO_4$	-0.3	14.95	41.7 (-0.2 V)	[11]
	Ru_{SAC}/C	0.05 M H_2SO_4	-0.2	120.9	29.6	[12]
	Ru_{SAC}/Mo_2CT_x	0.5 M K_2SO_4	-0.3	40.57	25.77	[13]
	MoS_2	0.1 M Li_2SO_4	-0.2	43.4	9.81	[14]
	Fe_{SAC}/C	0.1 M KOH	0.193	7.48	56.55	[15]
	$Mo\text{-}SnS_2$	0.5 M $LiClO_4$	-0.5	41.3	20.8 (-0.4 V)	[7]
	Pd_3Bi	0.05 M H_2SO_4	-0.2	59.05	21.52	[16]
	RuFeCoNiCu High-entropy alloys	0.1 M KOH	0.05	57.1	38.5	[17]
	$Cu\text{-}TiO_2$	0.5 M $LiClO_4$	-0.55	21.31	21.99	[18]
	$Fe\text{-}Ni_2P$	0.1 M HCl	-0.3	88.51	7.92	[19]
	NiSb	0.1 M HCl	-0.2	56.9	48 (-0.1)	[20]
	$PdH_{0.43}$	0.1 M PBS	-0.15	20.4	43.6	[21]
	Pd (100) cubes	0.1 M Li_2SO_4	0	24.3	36.6	[22]
	$Fe\text{-}W_{18}O_{49}$	0.25 M $LiClO_4$	-0.15	24.7	20	[23]
	$WeSe_{2-x}$	**0.5 m $LiClO_4$**	**-0.5**	**52.1**	**11.8 (-0.3 V)**	**This work**
Specific electrolytes	Fe-SS	Ionic liquid	-0.8	1.4	60	[24]
	$Fe@Fe_3O_4$	Ionic liquid	-0.6	0.72	32	[25]

	TiO_2	0.05 M H_2SO_4 with 20% PEG400	-0.3	36.38	32.13	[26]
	WSe_{2-x}	**12 m $LiClO_4$**	**-0.5**	**181.3**	**62.5 (-0.4 V)**	**This work**

Supplementary references

[1] Peterson, A. A., How Copper Catalyzes the Electroreduction of Carbon Dioxide into Hydrocarbon Fuels. *Energy Environ. Sci.* **2010,** 3, 1311-1315.

[2] Zhu, D.; Zhang, L.; Ruther, R. E.; Hamers, R. J., Photo-Illuminated Diamond as a Solid-State Source of Solvated Electrons in Water for Nitrogen Reduction. *Nat. Mater.* **2013,** 12, 836.

[3] Watt, G. W.; Chrisp, J. D., Spectrophotometric Method for Determination of Hydrazine. *Anal. Chem.* **1952,** 24, 2006-2008.

[4] Gu, W.; Guo, Y.; Li, Q.; Tian, Y.; Chu, K., Lithium Iron Oxide ($LiFeO_2$) for Electroreduction of Dinitrogen to Ammonia. *ACS Appl. Mater. Inter.* **2020,** 12, 37258-37264.

[5] Chu, K.; Liu, Y. P.; Li, Y. B.; Guo, Y. L.; Tian, Y., Two-Dimensional (2D)/2D Interface Engineering of MoS_2/C_3N_4 Heterostructure for Promoted Electrocatalytic Nitrogen Fixation. *ACS Appl. Mater. Inter.* **2020,** 12, 7081-7090.

[6] Chu, K.; Liu, Y.; Li, Y.; Guo, Y.; Tian, Y.; Zhang, H., Multi-Functional Mo-Doping in MnO_2 Nanoflowers toward Efficient and Robust Electrocatalytic Nitrogen Fixation. *Appl. Catal. B* **2020,** 264, 118525.

[7] Chu, K.; Wang, J.; Liu, Y. P.; Li, Q. Q.; Guo, Y. L., Mo-Doped SnS_2 with Rich S-Vacancies for Highly Efficient Electrocatalytic N_2 Reduction: The Critical Role of Mo-Sn-Sn Trimer. *J. Mater. Chem. A* **2020,** 8, 7117-7124.

[8] Qiu, W.; Xie, X.-Y.; Qiu, J.; Fang, W.-H.; Liang, R.; Ren, X.; Ji, X.; Cui, G.; Asiri, A. M.; Cui, G., High-Performance Artificial Nitrogen Fixation at Ambient Conditions Using a Metal-Free Electrocatalyst. *Nat. Commun.* **2018,** 9, 3485.

[9] Yang, C.; Huang, B.; Bai, S.; Feng, Y.; Shao, Q.; Huang, X., A Generalized Surface Chalcogenation Strategy for Boosting the Electrochemical N_2 Fixation of Metal Nanocrystals. *Adv. Mater.* **2020,** 32, 2001267.

[10] Lee, J.; Kumar, A.; Kim, M. G.; Yang, T.; Shao, X.; Liu, X.; Liu, Y.; Hong, Y.; Jadhav, A. R.; Liang, M., Single-Metal-Atom Dopants Increase the Lewis Acidity of Metal Oxides and Promote Nitrogen Fixation. *ACS Energy Lett.* **2021,** 6, 4299-4308.

[11] Li, Y.; Zhang, Q.; Li, C.; Fan, H.-N.; Luo, W.-B.; Liu, H.-K.; Dou, S.-X., Atomically Dispersed Metal Dimer Species with Selective Catalytic Activity for Nitrogen Electrochemical Reduction. *J. Mater. Chem. A* **2019,** 7, 22242-22247.

[12] Geng, Z.; Liu, Y.; Kong, X.; Li, P.; Li, K.; Liu, Z.; Du, J.; Shu, M.; Si, R.; Zeng, J., Achieving a Record-High Yield Rate of 120.9 μg_{NH3}^{-1} $\mu g_{cat.}^{-1}$ h^{-1} for N_2 Electrochemical Reduction over Ru Single-Atom Catalysts. *Adv. Mater.* **2018,** 30, 1803498.

[13] Peng, W.; Luo, M.; Xu, X.; Jiang, K.; Peng, M.; Chen, D.; Chan, T. S.; Tan, Y., Spontaneous Atomic Ruthenium Doping in Mo_2CT_x Mxene Defects Enhances Electrocatalytic Activity for the Nitrogen Reduction Reaction. *Adv. Energy. Mater.* **2020,** 10, 2001364.

[14] Liu, Y.; Han, M.; Xiong, Q.; Zhang, S.; Zhao, C.; Gong, W.; Wang, G.; Zhang, H.; Zhao, H., Dramatically Enhanced Ambient Ammonia Electrosynthesis Performance by in-Operando Created Li–S Interactions on Mos_2 Electrocatalyst. *Adv. Energy. Mater.* **2019,** 9, 1803935.

[15] Wang, M.; Liu, S.; Qian, T.; Liu, J.; Zhou, J.; Ji, H.; Xiong, J.; Zhong, J.; Yan, C., Over 56.55% Faradaic Efficiency of Ambient Ammonia Synthesis Enabled by Positively Shifting the Reaction Potential. *Nat. Commun.* **2019,** 10, 341.

[16] Wang, X.; Luo, M.; Lan, J.; Peng, M.; Tan, Y., Nanoporous Intermetallic Pd_3Bi for Efficient Electrochemical Nitrogen Reduction. *Adv. Mater.* **2021,** 33, 2007733.

[17] Zhang, D.; Zhao, H.; Wu, X.; Deng, Y.; Wang, Z.; Han, Y.; Li, H.; Shi, Y.; Chen, X.; Li, S., Multi-Site Electrocatalysts Boost pH-Universal Nitrogen Reduction by High - Entropy Alloys. *Adv. Funct. Mater.* **2021,** 31, 2006939.

[18] Wu, T.; Zhao, H.; Zhu, X.; Xing, Z.; Liu, Q.; Liu, T.; Gao, S.; Lu, S.; Chen, G.; Asiri, A. M.; Zhang, Y.; Sun, X., Identifying the Origin of Ti^{3+} Activity toward Enhanced Electrocatalytic N_2 Reduction over TiO_2 Nanoparticles Modulated by Mixed-Valent Copper. *Adv. Mater.* **2020,** 32, 2000299.

[19] Guo, C.; Liu, X.; Gao, L.; Kuang, X.; Ren, X.; Ma, X.; Zhao, M.; Yang, H.; Sun, X.; Wei, Q., Fe-Doped Ni_2P Nanosheets with Porous Structure for Electroreduction of Nitrogen to Ammonia under Ambient Conditions. *Appl. Catal. B* **2020,** 263, 118296.

[20] Fan, G.; Xu, W.; Li, J.; Chen, J. L.; Yu, M.; Ni, Y.; Zhu, S.; Su, X. C.; Cheng, F., Nanoporous NiSb to Enhance Nitrogen Electroreduction Via Tailoring Competitive Adsorption Sites. *Adv. Mater.* **2021,** 33, 2101126.

[21] Xu, W.; Fan, G.; Chen, J.; Li, J.; Zhang, L.; Zhu, S.; Su, X.; Cheng, F.; Chen, J., Nanoporous Palladium Hydride for Electrocatalytic N_2 Reduction under Ambient Conditions. *Angew. Chem. Int. Edit.* **2020,** 59, 3511-3516.

[22] Zhao, H.; Zhang, D.; Li, H.; Qi, W.; Wu, X.; Han, Y.; Cai, W.; Wang, Z.; Lai, J.; Wang, L., Exposure of Definite Palladium Facets Boosts Electrocatalytic Nitrogen Fixation at Low Overpotential. *Adv. Energy. Mater.* **2020,** 10, 2002131.

[23] Tong, Y.; Guo, H.; Liu, D.; Yan, X.; Su, P.; Liang, J.; Zhou, S.; Liu, J.; Lu, G. Q.; Dou, S. X., Vacancy Engineering of Iron-Doped $W_{18}O_{49}$ Nanoreactors for Low-Barrier Electrochemical Nitrogen Reduction. *Angew. Chem. Int. Edit.* **2020,** 59, 7356-7361.

[24] Zhou, F.; Azofra, L. M.; Ali, M.; Kar, M.; Simonov, A. N.; McDonnell-Worth, C.; Sun, C.; Zhang, X.; MacFarlane, D. R., Electro-Synthesis of Ammonia from Nitrogen at Ambient Temperature and Pressure in Ionic Liquids. *Energy Environ. Sci.* **2017,** 10, 2516-2520.

[25] Suryanto, B. H.; Kang, C. S.; Wang, D.; Xiao, C.; Zhou, F.; Azofra, L. M.; Cavallo, L.; Zhang, X.; MacFarlane, D. R., Rational Electrode-Electrolyte Design for Efficient Ammonia Electrosynthesis under Ambient Conditions. *ACS Energy Lett.* **2018,** 3, 1219-1224.

[26] Guo, Y.; Gu, J.; Zhang, R.; Zhang, S.; Li, Z.; Zhao, Y.; Huang, Z.; Fan, J.; Chen, Z.; Zhi, C., Molecular Crowding Effect in Aqueous Electrolytes to Suppress Hydrogen Reduction Reaction and Enhance Electrochemical Nitrogen Reduction. *Adv. Energy. Mater.* **2021,** 11, 2101699.